processes

MDPI

Article

Optimization of Thicknesses, Defect Density, and Bandgap in a Lead-Free $CsSnBr_3$/Silicon Two-Terminal Tandem Solar Cell via Simulation and Numerical Interpolation

Ezequiel Paz Totolhua [1], Mario Moreno Moreno [1,*], Javier Flores Méndez [2,3], Alfredo Morales Sánchez [1], Ana C. Piñón Reyes [2,3], Luis Hernández Martínez [1], Gabriel Omar Mendoza Conde [1], Zaira Jocelyn Hernández Simón [4], Jesús Carrillo López [4] and José Alberto Luna López [4,*]

[1] Coordinación de Electrónica, Instituto Nacional de Astrofísica, Óptica y Electrónica (INAOE), Luis Enrique Erro #1, Santa María Tonanzintla, Puebla 72840, Mexico; epaz@inaoep.mx (E.P.T.); alfredom@inaoep.mx (A.M.S.); luish@inaoep.mx (L.H.M.); gomendoza@inaoep.mx (G.O.M.C.)
[2] Área de Ingeniería, Benemérita Universidad Autónoma de Puebla (BUAP), Ciudad Universitaria, Blvd. Valsequillo y Esquina, Av. San Claudio s/n, Col. San Manuel, Puebla 72570, Mexico; javier.floresme@correo.buap.mx (J.F.M.); anacecilia.pinon@puebla.tecnm.mx (A.C.P.R.)
[3] Tecnológico Nacional de México/I.T. Puebla, Av. Tecnológico No. 420, Maravillas, Puebla 72220, Mexico
[4] Centro de Investigaciones en Dispositivos Semiconductores (CIDS-ICUAP), Benemérita Universidad Autónoma de Puebla (BUAP), Col. San Manuel, Cd. Universitaria. Av. San Claudio y 14 Sur, Puebla 72570, Mexico; zaira.hernandez@alumno.buap.mx (Z.J.H.S.); jesus.carrillolopez@viep.com.mx (J.C.L.)
* Correspondence: mmoreno@inaoep.mx (M.M.M.); jose.luna@correo.buap.mx (J.A.L.L.)

Abstract

This research study conducts a computational analysis of a two-terminal (2T) Perovskite-on-silicon (PVK-Si) solar cell with a tandem configuration. The motivation for this analysis arises from the outstanding potential of PVK-Si solar cells to surpass the efficiency limitations of conventional photovoltaic technology. The tandem configuration utilizes a combination of $CsSnBr_3$ in the top sub-cell and crystalline silicon (c-Si) in the bottom sub-cell. After optimizing parameters of the top sub-cell ($FTO/TiO_2/CsSnBr_3/rGO/Au$), which included the thicknesses of $CsSnBr_3$ (500 nm), TiO_2 (40 nm), rGO (50 nm), the interface defects (10^{13} cm^{-2}), and the bandgap of $CsSnBr_3$ (1.78 eV), the PVK-Si tandem device was simulated. As a result, the top $CsSnBr_3$ sub-cell achieved an efficiency of 21.62%, while the bottom silicon sub-cell achieved an efficiency of 23.48%. Subsequently, the sub-cells were interconnected in series using filtered spectra and current-density matching. After interpolating the J-V curves, the tandem exhibited a global efficiency of 29.76%, a fill factor (FF) of 85.30%, a matched current density (J_{SC}) of 19.02 mA/cm^2, and an open-circuit voltage (V_{OC}) of 1.83 V. The EQE results confirmed efficient photon management via complementary sub-cell absorption. The performance is competitive with experimental lead-based tandems and exceeds that of current lead-free simulations. Therefore, this research proposes a viable pathway for the development of non-toxic, cost-effective tandem solar systems with manufacturing capabilities.

Keywords: perovskite-on-silicon tandem solar cell; lead-free perovskite; silicon; defect density; current density matching; numerical interpolation

Academic Editor: Iván García Kerdan

Received: 27 February 2026
Revised: 22 April 2026
Accepted: 26 April 2026
Published: 28 April 2026

1. Introduction

The highest power conversion efficiency (PCE) of a single-junction perovskite solar cell (PSC) was 27.3% in 2025. To achieve a PCE close to the Shockley–Queisser theoretical

limit (~33%), it is important to minimize losses from thermalization and transmission [1]. The most promising alternative to overcome that limit is the use of multi-junction (or tandem) solar cells by combining light-absorbing materials with different bandgaps. As a noteworthy option, PVK-Si solar cells obtained 13.7% efficiency in 2015 and 34.6% efficiency in 2024 [2]. Their design enhances the utilization of the solar spectrum, as the top sub-cell absorbs photons with more energy, while the bottom sub-cell absorbs photons with less energy [3].

There are two main configurations for tandem devices. The first is the monolithic two-terminal (2T) configuration, which integrates two solar cells into a single stacked structure, sharing a substrate and an internal interconnection layer, resulting in a device with two contacts. The second is the four-terminal (4T) configuration, which manufactures the two cells independently and integrates them mechanically. Consequently, the 2T configuration is considered the most practical option for manufacturing due to its cost-effectiveness, reduced optical losses, and the absence of physical space between the two connected sub-cells [4]. Based on photovoltaic principles, the open-circuit voltage (V_{OC}) in a PVK-Si tandem solar cell is approximately equal to the sum of the V_{OC} of the two sub-cells, where losses are attributed to recombination in the contact layer of the interconnection. Conversely, the short-circuit current density (J_{SC}) of the tandem cell adheres to Kirchhoff's law. In other words, the V_{OCs} of the sub-cells are added together, and the J_{SC} is the same for the sub-cells [5].

Perovskite materials have the structural formula ABX_3. The most common halide anions (X) in this formula are chlorine (Cl), bromine (Br), and iodine (I). The metal cation (B) is usually lead (Pb) or tin (Sn). The cation (A) can be an inorganic substance, such as rubidium (Rb) or cesium (Cs), or an organic substance, such as methylammonium (MA) or formamidinium (FA). However, these materials, particularly lead-based compounds, which are used extensively, exhibit problems with their widespread use, including chemical instability and, more significantly, lead toxicity [6]. Recycling practices, life cycle evaluations, practical testing, and theoretical modeling are all necessary to determine and reduce the environmental impacts of new technologies [7]. Simultaneously, investigations are being conducted on Pb-free perovskites, with a particular focus on those incorporating Sn.

This study employed cesium tin bromide ($CsSnBr_3$) as a replacement for lead-based perovskite materials. This material exhibits a wide bandgap (~1.75), along with excellent thermal stability, extended carrier lifetime, and a high absorption coefficient, making it a promising candidate for PVK-Si tandem applications [8]. Nevertheless, the stability of PSCs containing Sn is compromised due to the formation of defects within the perovskite bulk. These defects can arise from moisture and oxygen exposure during material synthesis, adversely affecting stability and performance [9]. In addition, the Sn^{2+} propensity for oxidization could potentially diminish their efficacy. Research findings indicate that the incorporation of tin fluoride (SnF_2) into the precursor solution modifies the chemical and electrical properties of $CsSnBr_3$. These observations suggest that the inclusion of SnF_2 mitigates the oxidation of Sn (II) to Sn (IV), enhances substrate coverage, and diminishes carrier density by neutralizing traps [10].

The $CsSnBr_3$ perovskite was utilized as the absorber layer for the top sub-cell. Titanium dioxide (TiO_2) served as the electron transport layer (ETL), whereas reduced graphene oxide (rGO) served as the hole transport layer (HTL). In this context, TiO_2 exhibits favorable properties, such as good chemical stability, a wide bandgap (~3.2 eV) that ensures transparency in the visible spectrum, and suitable energy level alignment with perovskites for efficient electron extraction [11]. Additionally, rGO possesses essential attributes, including exceptional electrical conductivity, high optical transparency with a thin film form, optimal energy level alignment with lead-free perovskites, superior hole mobility, mechani-

cal flexibility, and enhanced thermal and chemical stability compared to Spiro-OmeTAD. In contrast to conventional HTLs like Spiro-OMeTAD, rGO enhances the stability and longevity of PSCs while also being significantly more cost-effective [12–14]. The incorporation of TiO_2/rGO with $CsSnBr_3$ simplifies the formation of a resilient structure that optimizes charge extraction, preserves high transparency for the unabsorbed solar spectrum, and enhances device longevity. These parameters are essential for the development of commercial PVK-Si tandem solar cells.

The simulations were conducted using the SCAPS-1D software package (version 3.3.11; University of Gent, Ghent, Belgium), initiated with the optimization of the top perovskite sub-cell based on an FTO/TiO_2/$CsSnBr_3$/rGO/Au structure. In order to achieve an improved power conversion efficiency for the standalone top sub-cell, the thicknesses of the HTL, ETL, and absorber layers were systematically varied, as were the defect densities in the absorber layer and interfaces, and the bandgap of $CsSnBr_3$ was adjusted. The results of this study showed that the standalone top sub-cell reached a PCE of 21.62%, with FF = 84.22%, J_{SC} = 21.96 mA/cm^2, and V_{OC} = 1.16 V.

The bottom silicon sub-cell has been simulated and optimized by varying the defect density at the interfaces: c–Si(n)/c–Si(p) and c–Si(p)/c–Si(p^+). Additionally, the shallow uniform donor densities (N_D and N_A) were adjusted. It should be noted that this research did not include optimization for the bottom sub-cell, as this has been thoroughly examined in previous studies [15,16].

The standalone bottom sub-cell had a PCE of 23.48%, with FF = 84.35%, J_{SC} = 39.40 mA/cm^2, and V_{OC} = 0.70 V. Subsequently, a method for matching current density was used on the PVK-Si tandem design [17,18]. In this process, the thickness of the perovskite absorber layer was modified according to a predetermined procedure, and the bottom silicon sub-cell was simulated with a filtered spectrum that corresponded to each perovskite thickness. The optimal J_{SC} matching condition was determined to be when the $CsSnBr_3$ layer was 200 nm thick, and the silicon layer was 278 µm thick. This led to a matched J_{SC} of 19.02 mA/cm^2 in both sub-cells.

After considerable analysis, the current-voltage (J-V) and external quantum efficiency (EQE) curves of the tandem device were obtained through the numerical interpolation of the individual J-V and EQE curves of the sub-cells. The resultant lead-free PVK-Si tandem solar cell exhibited an impressive PCE of 29.76%, with an FF of 85.30%, a V_{OC} of 1.83 V, a J_{SC} of 19.02 mA/cm^2, and excellent external quantum efficiency (EQE), confirming the broad-spectrum utility of the proposed architecture. The performance achieved by our proposed device is competitive with conventionally manufactured and simulated PVK-Si 2T tandem devices. In the context of lead-free tandem devices, there is currently a scarcity of experimental studies; consequently, our results constitute a necessary contribution to this line of research. This study emphasizes the potential of lead-free devices as a promising path toward non-toxic and potentially cost-effective photovoltaic technologies with long-term commercial viability.

2. Device Structure and Simulation Methodology

The proposed monolithic PVK-Si tandem architecture integrates two complementary sub-cells in a two-terminal configuration. As illustrated in Figure 1a, the top lead-free perovskite sub-cell consists of the following layer sequence: fluorine-doped tin oxide (FTO) as transparent front contact—compact TiO_2 (or SnO_2) as ETL/$CsSnBr_3$ as absorber—rGO as HTL—gold (Au) as back contact. Conventional *n-i-p* architecture was specifically chosen for this study as it provides a robust, well-established benchmark for evaluating the performance of emerging lead-free perovskites, such as $CsSnBr_3$. While *p-i-n* (inverted) structures have demonstrated high efficiencies in certain systems, the *n-i-p* configuration

allows for a more direct evaluation of charge transport properties using traditional electron transport materials (ETLs) such as TiO_2 and SnO_2 [5,6]. These materials are crucial for the initial optimization of novel perovskite compositions.

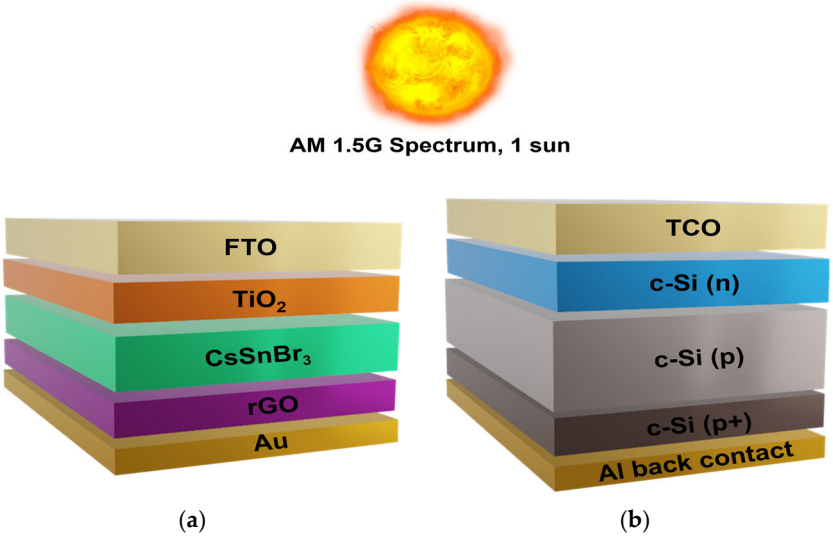

Figure 1. Schematic depiction of the (**a**) $CsSnBr_3$ top sub-cell and the (**b**) silicon bottom sub-cell under the AM1.5G 1 sun spectrum.

The bottom sub-cell, shown in Figure 1b, employs a p-type crystalline silicon homojunction with a back surface field (BSF). Its structure comprises the following: transparent front contact/n-type c-Si emitter layer/p-type c-Si base/heavily doped p^+ c-Si BSF layer/aluminium (Al) full-area back contact. The silicon bottom sub-cell supports two primary configurations: n–p–p or n–n–p doping profiles. Both use a front n^+ emitter as an electron-selective contact and a rear p^+ BSF as a hole-selective contact. This property facilitates the separation of carriers [19].

The individual sub-cells were simulated under the AM 1.5G 1 sun spectrum. However, for the proposed PVK-Si tandem device, the top sub-cell was simulated under the AM1.5G 1 sun spectrum and the bottom sub-cell was simulated under the spectrum filtered by the top perovskite sub-cell. Therefore, the present simulation model is designed to replicate the operational conditions of a tandem device [20]. Figure 2 illustrates a schematic of the simulated lead-free PVK-Si tandem device using this approach.

Numerical simulations were performed using the SCAPS-1D software (version 3.3.11; University of Gent, Ghent, Belgium), which is a Solar Cell Capacitance Simulator. This platform enables the modelling of single-junction or tandem devices with multilayer architectures comprising up to seven semiconductor layers by numerically solving the fundamental semiconductor equations under steady-state conditions [21]. The software can solve Poisson's equation, the continuity equations for holes and electrons, the charge transport equations, and the optical absorption coefficient. Each equation is elaborated upon in detail below. Poisson's equation is expressed as [22]

$$\frac{\partial^2 \Psi}{\partial x^2} = -\frac{dE}{dx} = -\frac{q}{\varepsilon_s}\left[p(x) - n(x) + N_d^+(x) - N_a^-(x) \pm N_{def}\right] \quad (1)$$

where q is the electron charge, ε_s is the permittivity of the absorber, $p(x)$ is the hole concentration, $n(x)$ is the electron concentration, and N_a^- and N_d^+ are the densities of ionized acceptors and donors, respectively. The continuity equations for holes and electrons are as follows [21,22]:

$$\frac{\partial p}{\partial t} = -\frac{1}{q}\nabla \cdot J_h + G(x) - R(x) \quad (2)$$

$$\frac{\partial n}{\partial t} = \frac{1}{q}\nabla \cdot J_e + G(x) - R(x) \tag{3}$$

where J_h is the hole current density, J_e is the electron current density, $G(x)$ is the carrier generation rate, and $R(x)$ is the recombination rate. The electron and hole transport equations are given by [21,22]

$$J_e = qn(x)\mu_e \frac{dv(x)}{d(x)} + qD_e \frac{dn(x)}{dx} \tag{4}$$

$$J_h = -qp(x)\mu_h \frac{dv(x)}{d(x)} - qD_h \frac{dp(x)}{dx} \tag{5}$$

where D_e and D_h are the diffusion constants for electrons and holes, respectively, and μ_e and μ_h are the electron and hole mobilities, respectively. The equation for the optical absorption coefficient is given by [21]

$$\alpha(\lambda) = \left(A + \frac{B}{hv}\right)\sqrt{hv - E_g} \tag{6}$$

where A and B are constants, E_g is the bandgap of the absorbing layer, h is Planck's constant, and v is the frequency of the photons. The spectrum filtered by the top sub-cell for different thicknesses of the $CsSnBr_3$ perovskite is calculated using the following equation [18]:

$$S_f(\lambda) = S_i(\lambda) \cdot \exp\left(\sum_{i=1}^{4} -\alpha_{mat_i}(\lambda) d_{mat_i}\right) \tag{7}$$

$S_f(\lambda)$ denotes the intensity of the spectrum filtered by the top sub-cell of $CsSnBr_3$, $S_i(\lambda)$ indicates the intensity of the incident light from the standard AM1.5G 1 sun spectrum (W/m^2), α_{mat_i} signifies the absorption coefficient of the respective material (cm^{-1}), d_{mat_i} indicates the thickness (cm), and the subscript mat_i refers to any specific material (where $i = 1, 2, 3, 4$ corresponds to TCO, ETL, perovskite, and HTL materials, respectively).

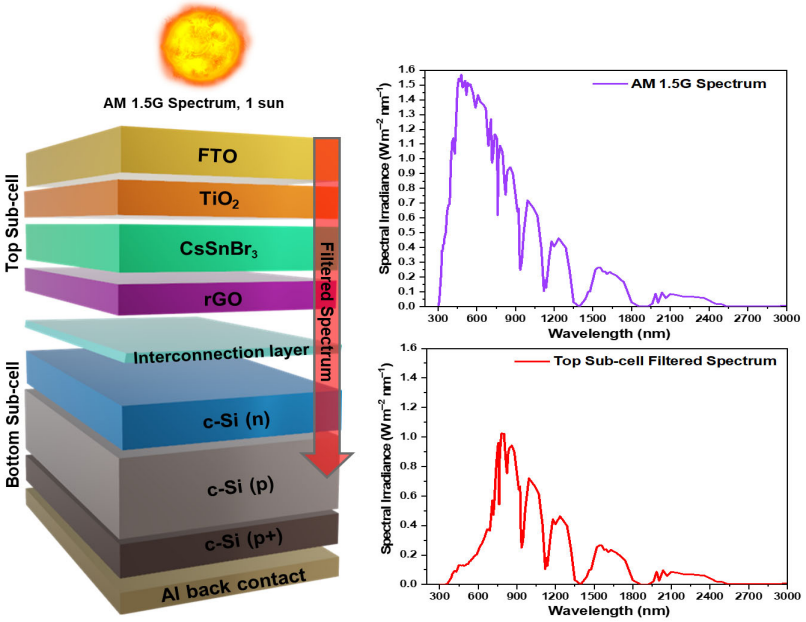

Figure 2. Schematic diagram of the proposed lead-free PVK-Si tandem solar cell, where the top sub-cell is illuminated by the AM 1.5G 1 sun spectrum and the bottom sub-cell is illuminated by the spectrum filtered by the top sub-cell.

To achieve current density matching, the thickness of the perovskite absorber layer was systematically varied from 100 nm to 700 nm, in 50 nm increments. This process generated a set of filtered spectra for the bottom sub-cell, as illustrated in Figure 3, following the high-resolution AM 1.5G standard [23]. Consequently, the optimal thickness combination was determined by identifying the current-matching point, plotting J_{SC} as a function of thickness for each absorber ($CsSnBr_3$ and c–Si). The filtered spectra obtained were used for this purpose [24,25]. This graph is presented and analyzed in the results section of the PVK-Si tandem solar cell simulation.

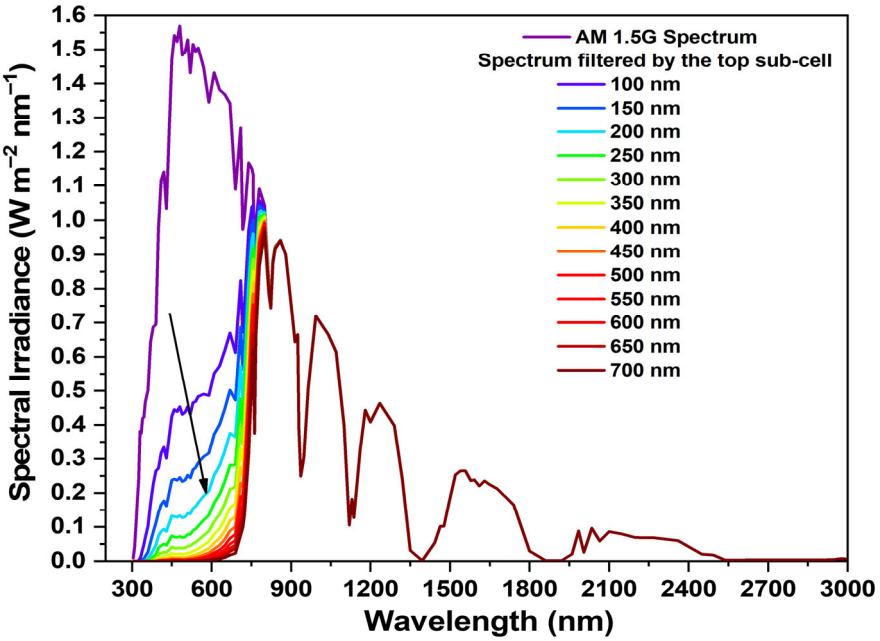

Figure 3. Spectra filtered for the bottom sub-cell using different thicknesses of $CsSnBr_3$ perovskite. The arrow indicates the progressive attenuation of the spectral irradiance in the visible region as the perovskite thickness increases, resulting from the enhanced photon absorption by the top sub-cell.

The simulation parameters for each layer of the lead-free PVK-Si tandem solar cell were derived from a comprehensive literature review of the optical and electrical properties of the materials [14,20,26–33]. Table 1 summarizes the key parameter values for the top and bottom sub-cells. Some of these values were adjusted during the optimization process for the top sub-cell, as detailed in the following section.

Except for the absorber perovskite, the layers were modeled with neutral defects and a single energy distribution. This distribution is characterized by an electron and hole capture cross section of 1×10^{-15} cm^2 and an energy level of 0.6 eV.

The interfaces ($TiO_2/CsSnBr_3$ and $CsSnBr_3/rGO$) were numerically modeled with neutral defects exhibiting Gaussian energy distribution, characterized by an electron and hole capture cross section of 1×10^{-19} cm^2, an energy level of 0.85 eV, and an initial defect density of 1×10^{-15} cm^2.

The interfaces for the silicon cell (c–Si(n)/c–Si(p) and c–Si(p)/c–Si(p^+)) were numerically modeled with deep-level neutral defects located near the middle of the bandgap with an electron and hole capture cross section of 1×10^{-15} cm^2 and an initial defect density of 1×10^{-15} cm^2.

Table 1. Optical and electrical characteristics of the materials employed in the top and bottom sub-cells of the PVK-Si tandem device.

Parameters	FTO	TiO_2	SnO_2	$CsSnBr_3$	rGO	c–Si (n)	c–Si (p)	c–Si (p^+)
References	[20,26]	[27,28]	[33]	[28,30]	[29,30]	[14,31,32]	[14,31,32]	[14,31,32]
Thickness	500 nm	120 nm	50 nm	300 nm	100 nm	0.5 µm	200 µm	10 µm
Bandgap, Eg (eV)	3.5	3.2	3.5	1.75	1.69	1.12	1.12	1.12
Electron affinity, χ (eV)	4	4	4	4.07	3.56	4.05	4.05	4.05
Dielectric permittivity, ε_r	9	9	9	5.9	13.3	11.9	11.9	11.9
CB, effective density of states (cm^{-3})	2.02×10^{18}	2.0×10^{18}	2.2×10^{18}	1.0×10^{19}	1.8×10^{18}	2.8×10^{19}	2.8×10^{19}	2.8×10^{19}
VB, effective density of states (cm^{-3})	1.8×10^{19}	1.8×10^{19}	1.8×10^{19}	1.0×10^{19}	1.8×10^{19}	1.04×10^{19}	1.04×10^{19}	1.04×10^{19}
Electron thermal velocity (cm/s)	1.0×10^{7}	1.0×10^{7}	1.0×10^{7}	1.0×10^{7}	1.0×10^{7}	1.0×10^{7}	1.0×10^{7}	1.0×10^{7}
Hole thermal velocity (cm/s)	1.0×10^{7}	1.0×10^{7}	1.0×10^{7}	1.0×10^{7}	1.0×10^{7}	1.0×10^{7}	1.0×10^{7}	1.0×10^{7}
Electron mobility, μ_n ($cm^2\ V^{-1}\ S^{-1}$)	20	20	100	2	26	1400	1400	1400
Hole mobility, μ_p ($cm^2\ V^{-1}\ S^{-1}$)	0.1	10	25	2	123	450	450	450
Shallow uniform donor density, N_D (cm^{-3})	2.0×10^{19}	9.0×10^{16}	1.0×10^{17}	0	0	1.0×10^{20}	0	0
Shallow uniform acceptor density, N_A (cm^{-3})	0	0	0	1.0×10^{15}	1.0×10^{22}	0	1.5×10^{16}	1.0×10^{20}
Defect type	Neutral	Neutral	Neutral	Neutral	Neutral	Neutral	Neutral	Neutral
Capture cross section electrons (cm^2)	1.0×10^{-15}	1.0×10^{-15}	1.0×10^{-15}	1.0×10^{-15}	1.0×10^{-15}	1.0×10^{-15}	1.0×10^{-15}	1.0×10^{-15}
Capture cross section holes (cm^2)	1.0×10^{-15}	1.0×10^{-15}	1.0×10^{-15}	1.0×10^{-15}	1.0×10^{-15}	1.0×10^{-15}	1.0×10^{-15}	1.0×10^{-15}
Energetic distribution	Single	Single	Single	Gaussian	Single	Single	Single	Single
Reference for defect energy level E_t	Above Ev	Above Ev	Above Ev	Above Ev	Above Ev	Above Ev	Above Ev	Above Ev
Energy level with respect to reference (eV)	0.6	0.6	0.6	0.85	0.6	0.6	0.6	0.6
Defect density, N_t total (cm^{-3})	1.0×10^{15}	1.0×10^{15}	1.0×10^{15}	1.0×10^{17}	1.0×10^{15}	1.0×10^{12}	1.0×10^{12}	1.0×10^{12}

The capture cross-section values for electrons and holes were selected based on ranges commonly reported in the literature for defect-assisted recombination. For bulk defects in both perovskite and crystalline silicon, values on the order of 10^{-15} cm^2 were used. For interface defects, different values were adopted depending on the material system. In the perovskite top sub-cell, lower capture cross-section values (10^{-19} cm^2) were employed to represent the reduced recombination activity associated with partially passivated interfaces. In contrast, for the silicon bottom sub-cell, interface capture cross-sections were set in the range of 10^{-16}–10^{-15} cm^2 to reflect the higher recombination activity typically observed at crystalline silicon interfaces, particularly at unpassivated contacts [34,35].

The interconnection layer was modeled as an ideal recombination interface with perfect electron-hole recombination. Negligible optical and electrical losses were assumed. As the layer is optically transparent, it does not significantly affect the light transmitted to the bottom silicon sub-cell. This approach is commonly adopted in SCAPS-1D-based simulations of tandem solar cells to decouple the intrinsic performance of the sub-cells from the additional complexities introduced by the interconnection layer; therefore, no parameters for this layer were included [17,18]. The results presented in this work represent an upper-limit estimate of the device performance.

The absorption coefficient data for the top sub-cell were obtained from the literature and are illustrated in Figure 4 [10,36–38]. Variations in this parameter within the perovskite absorber ($CsSnBr_3$) primarily affect the photogenerated current density of the top sub-cell, whereas the transport layers (TiO_2 and rGO) and the FTO have a smaller impact, mainly associated with parasitic losses. The absorption coefficients of the bottom c-Si sub-cell were obtained from the simulation software database. The standalone simulations were performed at 300 K under standard AM 1.5G, 1-sun illumination.

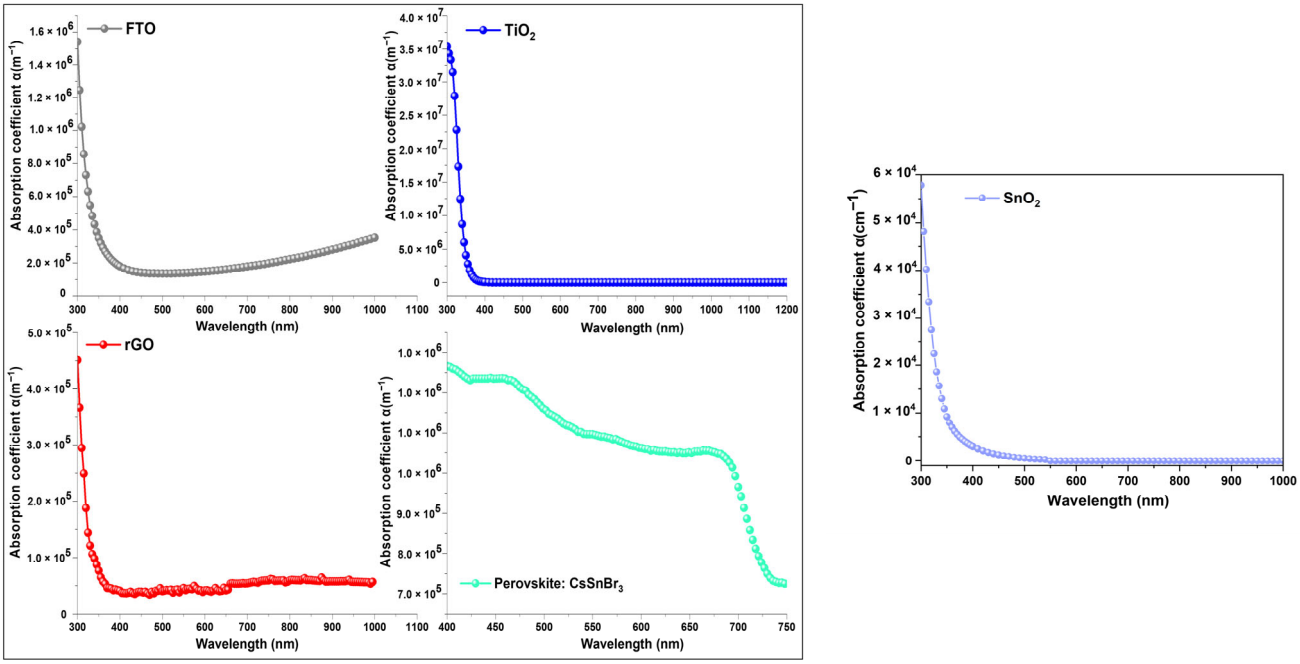

Figure 4. Absorption models of the FTO, TiO_2, SnO_2, $CsSnBr_3$, and rGO materials for the top sub-cell. Data compiled from references [10,36–38] and processed by the authors.

3. Results and Discussion

3.1. Effect of Perovskite Thickness and Defects on the Performance of the Top Sub-Cell

Adjusting the thickness of the perovskite layer in the top sub-cell is essential, since it facilitates light absorption and the formation of electron-hole pairs. The correlation between the PCE and perovskite thickness is associated with the equilibrium of photon absorption and charge carrier recombination rates [39].

The thickness of the $CsSnBr_3$ varied from 50 nm to 1000 nm in this section. Figure 5a illustrates that when the thickness of $CsSnBr_3$ increases from 50 to 500 nm, PCE rises from 13.5% to 21.6%, J_{SC} increases from 13.73 mA/cm^2 to 21.96 mA/cm^2, FF diminishes from 87.13% to 84.12%, and V_{OC} experiences a minor increase from 1.142 V to 1.171 V. This phenomenon is caused by the enlarged volume of $CsSnBr_3$ material, which augments the photo-generated electron-hole pairs. For thicknesses between 500 nm and 1000 nm, there was a slight decrease in the PCE and J_{SC}, while the FF remained constant and the V_{OC} exhibited a modest increase. The reductions in PCE and J_{SC} can be attributed to the thickness-dependent increase in the travel distance of photo-generated charge carriers, which increases the possibility of recombination and consequently diminishes the lifetime of the charge carriers. This impacts the performance of the solar device [40]. The optimal thickness for the $CsSnBr_3$ layer was determined to be 500 nm for operation as an independent solar cell.

The defect density (N_t) in the $CsSnBr_3$ layer is a critical parameter that determines device performance in both standalone and tandem configurations. A high N_t concentration in the absorbing layer increases pinhole formation, accelerates layer degradation, reduces stability, enhances recombination processes, and deteriorates the device performance. The dual role of the absorber layer as the site for carrier generation and recombination makes control of N_t essential for achieving high efficiency [41]. Low N_t values are therefore recommended for optimal device performance.

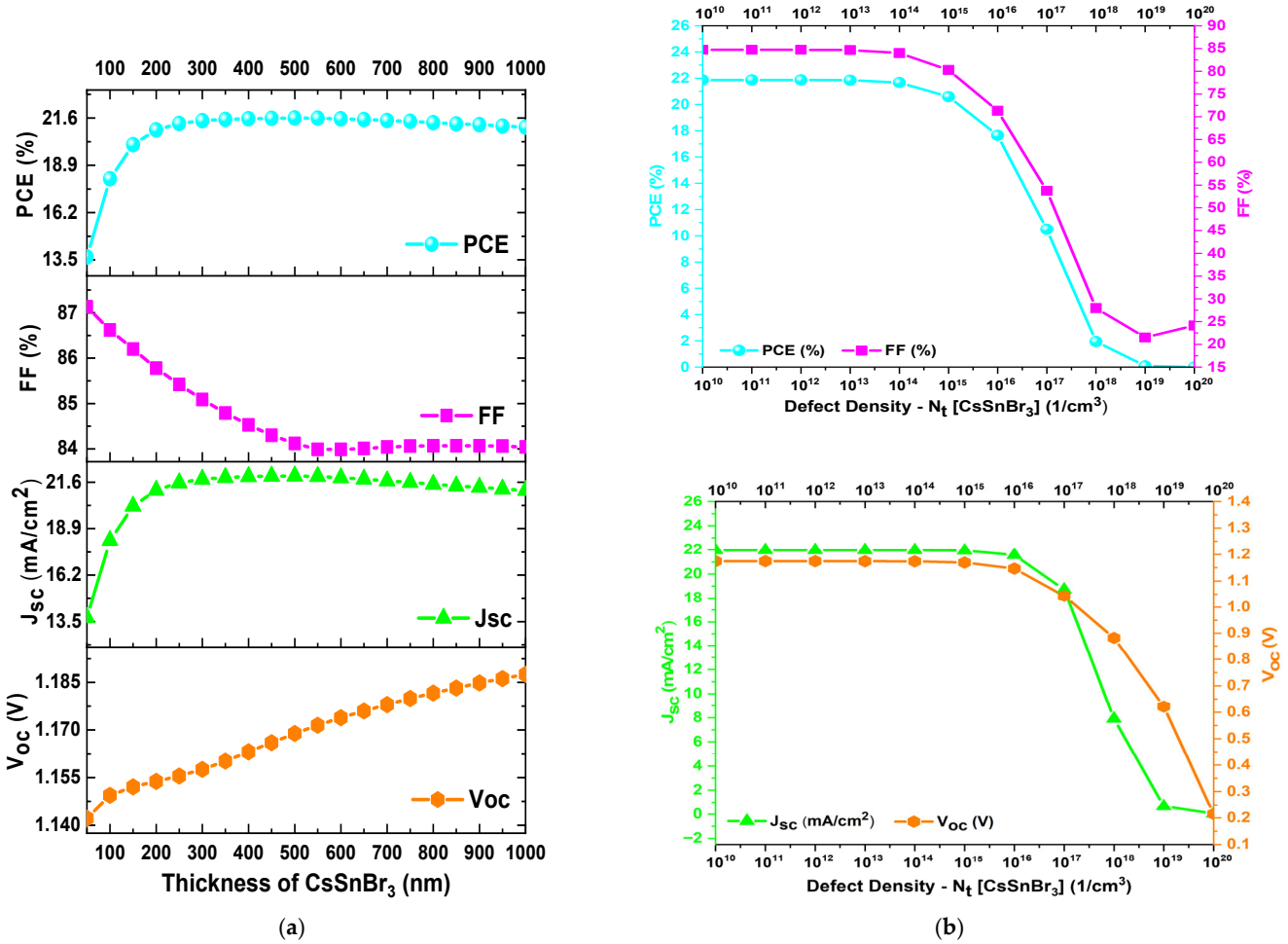

(**a**) (**b**)

Figure 5. Effect of (**a**) thickness and (**b**) N_t of the $CsSnBr_3$ layer on the P_{CE}, FF, J_{SC}, and V_{OC} parameters.

The perovskite bulk defect density is modelled using the Shockley–Read–Hall (SRH) recombination mechanism, represented by the following Equation (8) [42]:

$$R_{SRH} = \frac{np - n_i^2}{\tau_p\left(n + N_c e^{\frac{(E_g - E_t)}{kT}}\right) + \tau_n\left(p + N_v e^{\frac{E_t}{kT}}\right)} \tag{8}$$

where n and p correspond to the electron and hole concentrations, respectively; n_i is the intrinsic carrier concentration; E_t is the defect energy level; and $\tau_{p,n}$ represents the charge carrier lifetime.

According to the SRH recombination model, the carrier lifetime ($\tau_{p,n}$) and the diffusion length (L_D) exhibit an inverse dependence on the defect density (N_t). A larger value of $\tau_{p,n}$ indicates that recombination occurs less frequently. The values of $\tau_{p,n}$ and L_D are determined using the following equation [43]:

$$\tau_{n,p} = \frac{1}{N_t \delta v_{th}}; \; L_D = \sqrt{\frac{\mu_{(n,\,p)} kT}{q} \tau_{p,n}} \tag{9}$$

where δ is the capture cross-section for electrons and holes, v_{th} is the thermal velocity of the charge carriers, and $\mu_{(n,p)}$ is the electron and hole mobility.

An increase in N_t within the perovskite bulk introduces additional recombination centres, thereby reducing both $\tau_{p,n}$ and L_D. This degradation in transport properties directly compromises device performance, mainly in a reduction of V_{OC} and PCE [29].

The performance of the top sub-cell is contingent upon N_t, as demonstrated in Figure 5b. Analysis across a concentration range of 1×10^{10} cm^{-3} to 1×10^{20} cm^{-3} indicates that an increase in N_t adversely affects all photovoltaic metrics (PCE, FF, J_{SC}, and V_{OC}). This deterioration is ascribed to a decline in L_D and recombination processes within the perovskite [42]. As N_t escalates from 1×10^{14} cm^{-3} to 1×10^{20} cm^{-3}, a significant decline in all photovoltaic parameters is evident: PCE decays from 21.67% to 0.09%, FF diminishes from 83.99% to 24.11%, J_{SC} reduces from 21.97 mA/cm^2 to 0.048 mA/cm^2, and V_{OC} falls from 1.173 V to 0.214 V. Consequently, an optimal N_t value of 1×10^{14} cm^{-3} was used for both the independent simulation and the tandem simulation.

3.2. Effect of TiO_2, SnO_2, and rGO Thicknesses on the Performance of the Top Sub-Cell

This section is focused on optimizing the thickness of ETL and HTL. The TiO_2 layer was optimized by varying its thickness between 10 nm and 120 nm, while the parameters of the other layers were kept constant throughout the simulation. TiO_2 serves as both an ETL and a blocking layer, thereby preventing direct contact between holes and the FTO substrate. Furthermore, the thickness of the TiO_2 layer must be minimized to enable rapid electron transport and reduce resistivity losses [44].

Figure 6a shows that an increase in thickness from 10 nm to 120 nm resulted in a decline in PCE from 21.87% to 21.37%, while FF decreased from 84.99% to 82.95%. Notably, J_{SC} and V_{OC} remained essentially constant throughout the thickness range, with values of 21.978 mA/cm^2 and 1.179 V, respectively. The reduction in PCE and FF is attributed to the increased defect density (from increasing TiO_2 thickness), which diminishes electron mobility and diffusion length [45]. Figure 6a shows that while the highest efficiency is achieved at lower thicknesses, both V_{OC} and J_{SC} reach their maximum values at approximately 40 nm. Therefore, 40 nm was selected as the optimal thickness to ensure a balance between high carrier extraction and complete surface coverage. This thickness prevents shunt paths typically associated with ultra-thin layers while maintaining sufficient transparency for the bottom sub-cell [46].

In an alternative configuration for the top perovskite sub-cell, the thickness of the SnO_2 ETL was optimized within a range of 10 nm to 120 nm to evaluate its influence on the device's photovoltaic performance. As shown in Figure 6b, the SnO_2-based configuration exhibited a trend similar to that of TiO_2, where a gradual increase in thickness led to a decrease in PCE (from 21.72% to 21.62%) and J_{SC} (from 21.90 mA/cm^2 to 21.80 mA/cm^2). This degradation is primarily attributed to increased series resistance and higher recombination rates within the thicker ETL bulk. Notably, FF and V_{OC} remained nearly constant at 85.43% and 1.16 V, respectively. It is important to highlight that the SnO_2 layer maintained a higher FF across the entire range compared to TiO_2, suggesting superior electron extraction properties. Although the maximum PCE was observed at 10 nm, an optimal thickness of 20 nm was selected to ensure robust, pinhole-free interfacial coverage and to prevent shunting without compromising the high transparency required for tandem applications.

Meanwhile, rGO has emerged as a novel and promising material for use as an HTL in solar devices. The influence of the rGO layer thickness on PSC performance is critical. An excessively thick rGO layer has been demonstrated to reduce transparency by blocking photons, which are essential for the generation of charge carriers in the perovskite, leading to a drop in FF and a progressive decrease in PCE. Conversely, an extremely thin thickness will have non-homogeneous coverage, leading to high electrical resistance that will hinder the extraction of charge carriers, and, therefore, there cause a decrease in the J_{SC} and PCE values [47].

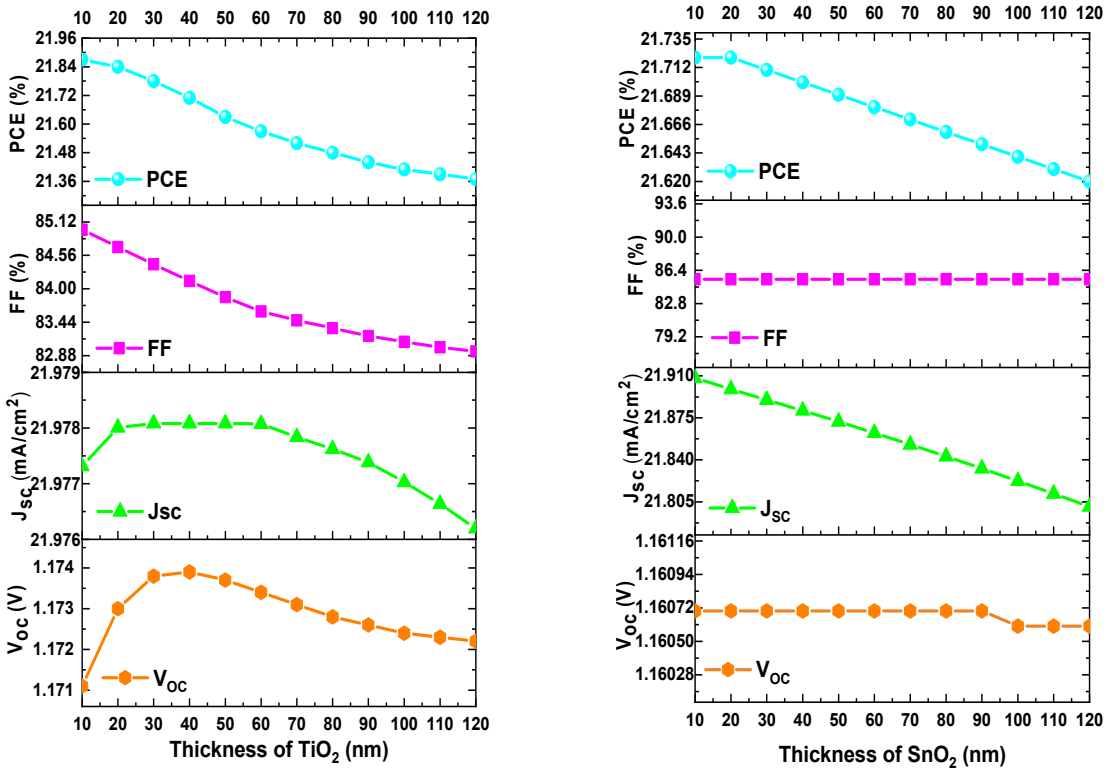

Figure 6. Effect of (**a**) TiO_2 thickness and (**b**) SnO_2 thickness on the PCE, FF, J_{SC}, and V_{OC} parameters.

In this section, the rGO layer used as the HTL was optimized by varying its thickness from 5 nm to 140 nm. As illustrated in Figure 7, the PCE exhibits a gradual increase from 21.64% to 21.74%, primarily driven by an enhancement in the J_{SC}, which rises from 21.92 mA/cm^2 to 22.09 mA/cm^2. In contrast, the FF shows a slight decline from 84.06% to 83.85%. Notably, the V_{OC} exhibits a slight step-up and stabilizes at approximately 50 nm, maintaining a constant value of 1.1739 V thereafter. This stabilization suggests that a minimum thickness of 50 nm is required to ensure complete surface passivation and film continuity. Therefore, 50 nm was selected as the optimal thickness to balance efficient hole extraction with the high optical transparency required for the silicon bottom sub-cell [47,48].

3.3. Effect of N_t Variation at the Interfaces on the Performance of the Top Sub-Cell

The quality of the interfaces is a decisive factor for the final performance of the solar cell. The presence of defects N_t at the interfaces, specifically in contact regions such as $TiO_2/CsSnBr_3$ and $CsSnBr_3$/rGO, produces energy states within the bandgap that act as Shockley–Read–Hall (SRH) recombination centers. Charge carrier recombination is the result of defects caused by deposition, such as chemical impurities, surface dislocations, sub-coordinated atoms, and dangling bonds [49]. This phenomenon is directly correlated with the degradation of key photovoltaic parameters, including V_{OC}, J_{SC}, FF, and PCE. The interfacial recombination rate ($R_{SRH,interface}$) is represented by the following Equation (10), which critically depends on the surface recombination velocities (δ_n and δ_p) and the total N_t [50]:

$$R_{SRH,interface} = \frac{n_t p_t - {n_i}^2}{\frac{p_t + N_v\, e^{\left(\frac{E_t}{kT}\right)}}{\delta_n} + \frac{n_t + N_c\, e^{\left(\frac{E_g - E_t}{kT}\right)}}{\delta_p}} \quad (10)$$

$$\delta_n = \sigma_n N_t \nu_{th} \quad (11)$$

$$\delta_p = \sigma_p N_t v_{th} \quad (12)$$

Here, E_t denotes the trap energy level, σ_n and σ_p represent the electron and hole capture cross-sections, respectively, v_{th} is the thermal velocity of the charge carriers, and n_t and p_t are the concentrations of carriers trapped at the interface [51]. As is the case with the bulk perovskite, an ideal interface is characterized by low N_t values, which directly lead to low surface recombination velocities (δ_n and δ_p). It is imperative to maintain these parameters at low values to maximize device performance.

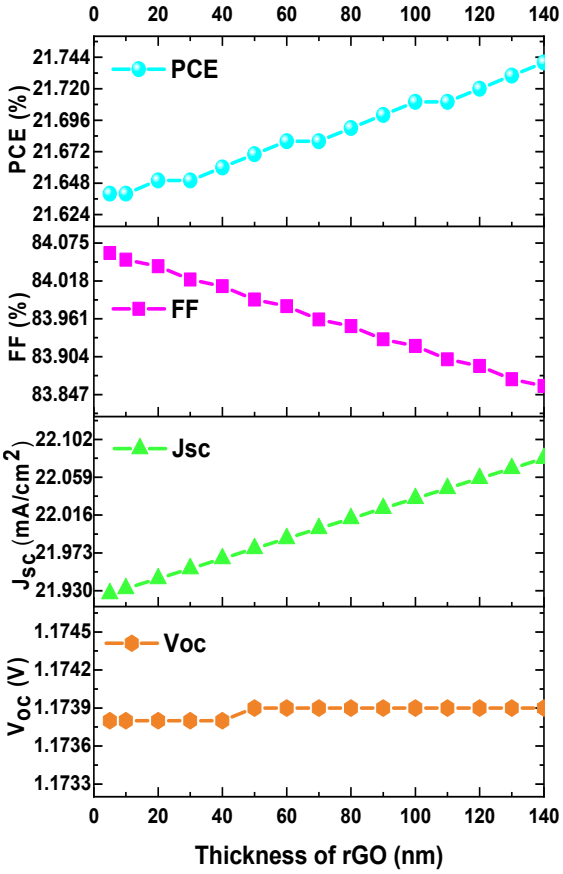

Figure 7. Effect of rGO thickness on the PCE, FF, J_{SC}, and V_{OC} parameters.

This section examines the impact of interfacial defect density on the performance of the top sub-cell. N_t was varied within the range of 10^{10} cm^{-2} to 10^{20} cm^{-2}, while all other parameters were kept constant throughout the simulation.

Figure 8 illustrates that all photovoltaic metrics (PCE, FF, J_{SC}, and V_{OC}) demonstrate incremental degradation with rising N_t at the TiO_2/$CsSnBr_3$ interface. A quantitative analysis reveals a decline in performance metrics as nitrogen concentration N_t escalates from 10^{10} cm^{-2} to 10^{20} cm^{-2}. Specifically, there is a decrease in the PCE from 21.67% to 11.18%, the FF declines from 83.99% to 65.74%, J_{SC} reduces from 21.97 mA/cm^2 to 15.99 mA/cm^2, and V_{OC} drops from 1.17 V to 1.06 V. The observations indicate that 10^{13} cm^{-2} is the ideal N_t value, delineating the threshold beyond which significant performance degradation occurs in the top sub-cell.

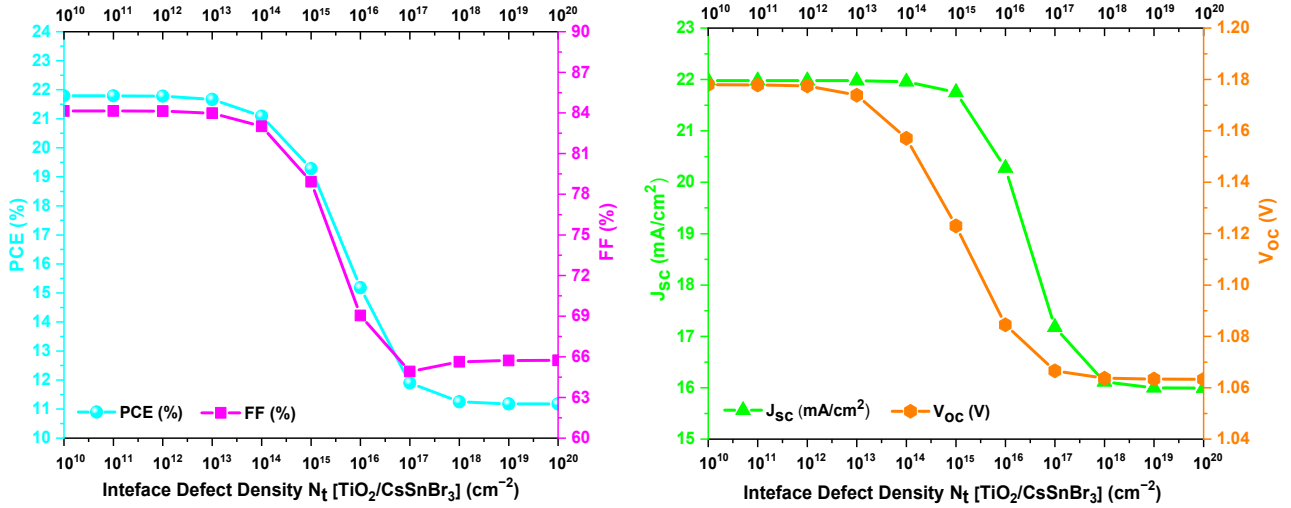

Figure 8. Effect of N_t at the $TiO_2/CsSnBr_3$ interface on the PCE, FF, J_{SC}, and V_{OC} parameters.

Figure 9 illustrates the effect of N_t at the $CsSnBr_3$/rGO interface on the photovoltaic parameters PCE, FF, J_{SC}, and V_{OC}. The analysis reveals that increasing N_t causes a slight degradation in sub-cell performance. To evaluate this effect, N_t was varied from 10^{10} cm^{-2} to 10^{20} cm^{-2}. The performance characteristics exhibited negligible variation compared with the $TiO_2/CsSnBr_3$ interface. The PCE decreased from 21.67% to 20.78%, V_{OC} decreased from 1.17 V to 1.15 V, J_{SC} decreased from 21.97 mA/cm^2 to 21.91 mA/cm^2, and FF decreased from 83.99% to 82.36%. However, in accordance with the criteria established in the previous interface, the value of 10^{13} cm^{-2} was identified as the optimal value.

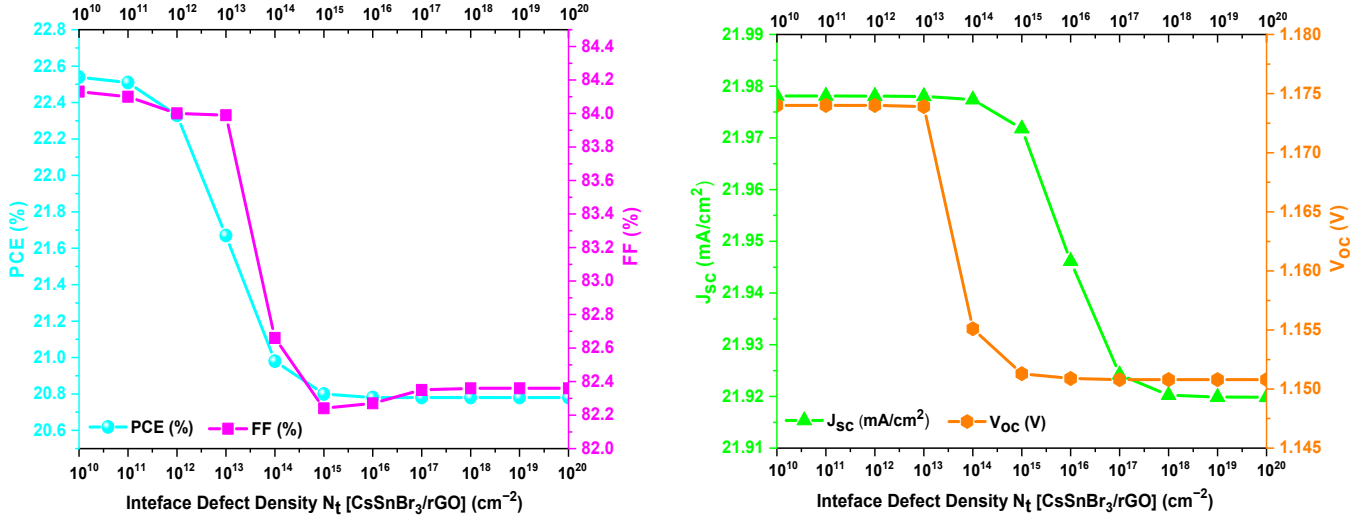

Figure 9. Effect of N_t at the $CsSnBr_3$/rGO interface on the PCE, FF, J_{SC}, and V_{OC} parameters.

3.4. Effect of Perovskite Bandgap (Eg) Variation on the Performance of the Top Sub-Cell

The bandgap (E_g) is an important property since it dictates the range of the solar spectrum that can be absorbed. Calibration of this parameter is imperative to enhance light absorption, thereby optimizing the performance of devices. The most common methods of producing this phenomenon include compositional and interface engineering, doping, dimensional alteration of the material, and applying pressure or strain [52]. This tuning is of particular significance in tandem cell structures, where solar cells with different band gaps are arranged in a stacking configuration to capture distinct segments of the solar

spectrum. The bandgap of the top sub-cell should be between 1.5 eV and 2.2 eV, while the bottom sub-cell bandgap should be between 0.9 eV and 1.2 eV [53].

In this section, we evaluate the impact of the E_g calibration of the $CsSnBr_3$ perovskite on the performance of the top sub-cell. As shown in Figure 10, the simulation range was restricted to 1.75–1.78 eV to strictly match the experimental values reported in the literature for $CsSnBr_3$ [8,52]. Throughout this range, the PCE remains exceptionally stable at approximately 21.62%, while FF shows a negligible decrease from 84.22% to 84.1%. The J_{SC} maintains a constant value close to 21.96 mA/cm^2, and the V_{OC} exhibits a slight upward trend, peaking at 1.78 eV. Although lower bandgaps near 1.7 eV are achievable using double-halide perovskites such as $CsSnIBr_2$—which have been experimentally demonstrated and simulated using SCAPS-1D—these could potentially improve current matching in tandem configurations [54,55]. However, $CsSnBr_3$ was selected for this study due to its well-established synthesis protocols and non-toxic nature [56]. Consequently, an E_g value of 1.78 eV was determined as the optimal parameter for the top sub-cell to ensure maximum efficiency and voltage in the tandem device.

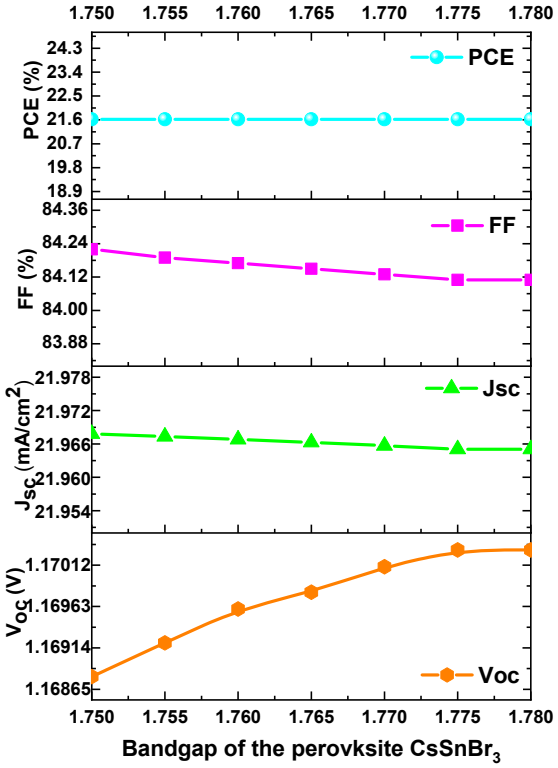

Figure 10. Effect of the $CsSnBr_3$ bandgap on the PCE, FF, J_{SC}, and V_{OC} parameters.

3.5. Independent Simulation of the Top and Bottom Sub-Cells

The final configuration of the optimized top perovskite sub-cells were defined by the following structures: FTO (500 nm)/TiO_2 (40 nm)/$CsSnBr_3$ (500 nm)/rGO (50 nm)/Au and FTO (500 nm)/SnO_2 (20 nm)/$CsSnBr_3$ (500 nm)/rGO (50 nm)/Au. Meanwhile, the optimized bottom silicon sub-cell structure was a homojunction composed of TCO/c–Si(n) 0.5 µm/c–Si(p) 200 µm/c–Si(p^+) 10 µm/Al. Independent simulations for both sub-cells were performed under the standard AM1.5G 1-sun spectrum, assuming ideal optical conditions without considering surface or interfacial reflectance losses. Figure 11a,b show the characteristic J-V curves and performance parameters for both optimized devices under these ideal assumptions.

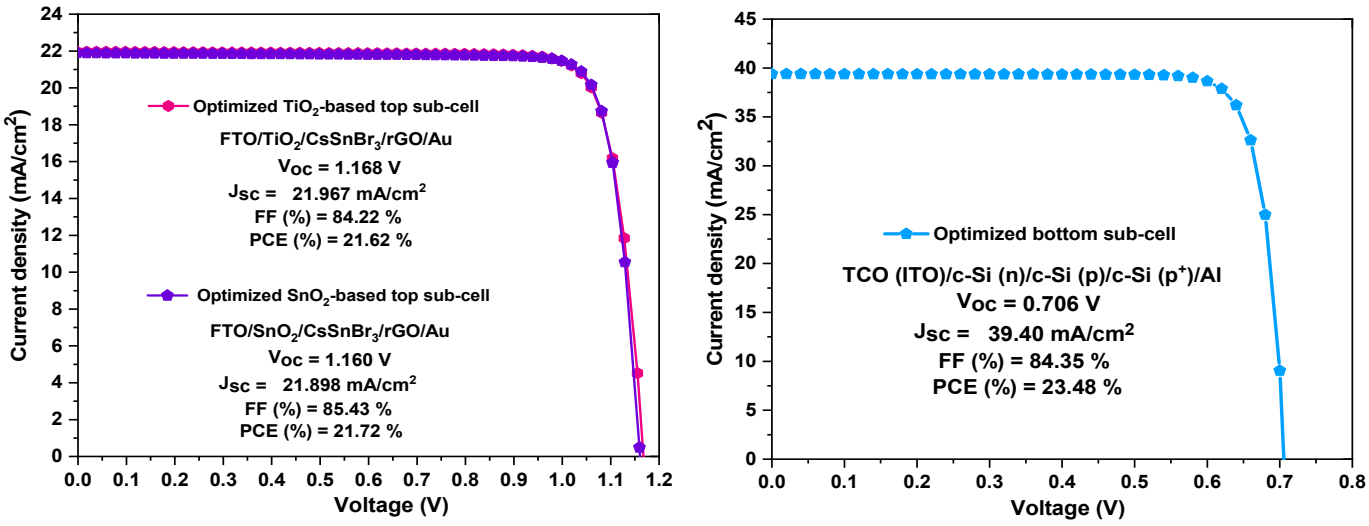

Figure 11. Characteristic J-V curves of the (**a**) perovskite top sub-cell and (**b**) silicon bottom sub-cell.

Figure 12a,b illustrate the energy band diagrams of the sub-cells. Figure 12a shows the conduction band (E_C), the valence band (E_V), and the quasi-Fermi levels for electrons and holes (F_n and F_p) in the top sub-cell. The band curvature of the $CsSnBr_3$ absorber layer demonstrates a slow change over time. This means that when light interacts with the layer, an electric field is generated internally, thereby maintaining the separation between the charge carriers. The diagram shows that the energy is well-aligned and the selective contacts are clear. This facilitates the efficient movement of carriers around the sub-cell. Furthermore, the energy band diagram of the bottom sub-cell (see Figure 12b) demonstrates that the curvature of the bands at the c-Si(n)/c-Si(p) interface confirms the formation of the p-n junction and the internal electric field that is responsible for carrier separation. The c-Si(p) layer acts as the main absorber, while the heavily doped c-Si (p+) region enables the selective extraction of holes toward the rear Al contact.

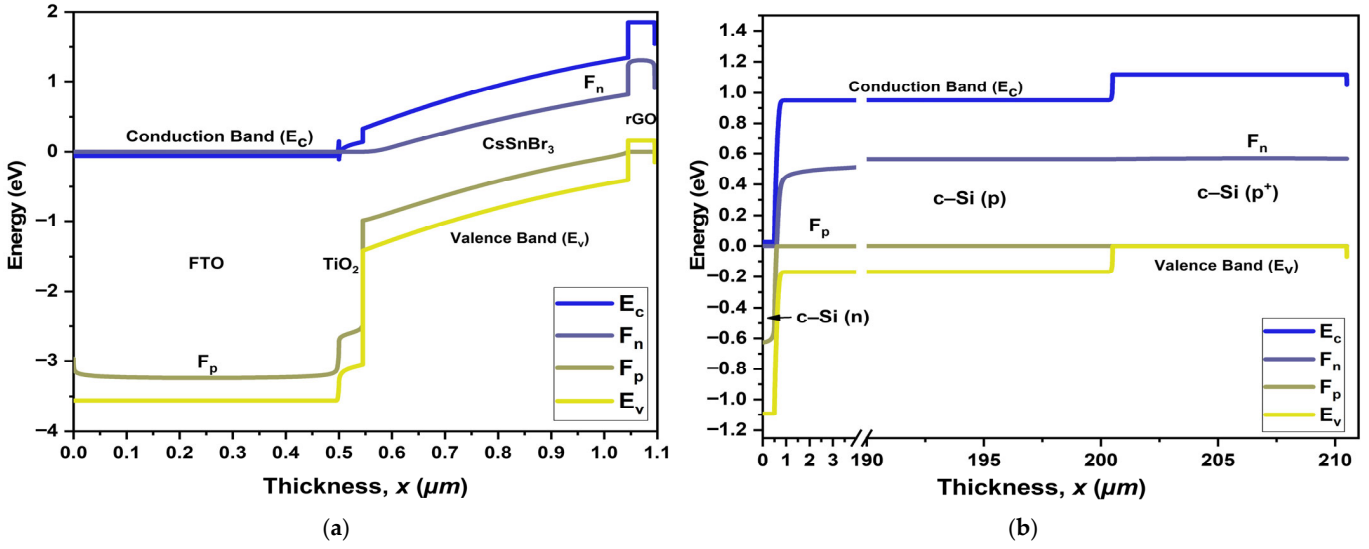

Figure 12. Simulated energy band diagrams of the (**a**) perovskite top sub-cell and (**b**) silicon bottom sub-cell.

The resulting energy alignment indicates efficient contact and favorable carrier transport. Taken together, both band diagrams demonstrate a suitable energy alignment for integration into a perovskite–silicon tandem architecture.

3.6. Effect of Optical Reflectance and Current Matching Optimization on the Performance of the Tandem Solar Cell

To improve the physical accuracy of the simulation, the impact of optical reflectance losses in both sub-cells was evaluated. In practical tandem devices, reflectance at the interfaces is a critical factor; the previous literature indicates that parasitic reflections can account for losses of approximately 1 mA/cm^2 in the perovskite region, while in high-efficiency silicon tandem solar cells, reflection losses ranging from 5% to 30% have been reported [57,58]. Based on these reports, a front reflectance (R_{front}) of 10% was assumed for the top perovskite sub-cell (configured with a TiO_2 ETL and a 200 nm $CsSnBr_3$ absorber), to account for cumulative reflection losses at the air/glass and glass/FTO interfaces. Meanwhile, an intermediate interfacial reflectance (R_{int}) of 20% was applied to the bottom sub-cell (278 µm of silicon). As illustrated in Figure 13a,b, these conditions resulted in a measurable reduction in photovoltaic parameters. The J_{SC} of the top sub-cell decreased from an ideal value of 21.13 mA/cm^2 to 19.02 mA/cm^2 upon introducing the 10% reflectance at the top contact. Similarly, for the bottom silicon sub-cell under the filtered spectrum, the J_{SC} decreased from 22.58 mA/cm^2 to 19.02 mA/cm^2 when applying the 20% intermediate interfacial reflectance. Under this conservative scenario, the current matching point was accurately identified at 19.02 mA/cm^2, where the top sub-cell exhibits a V_{OC} of 1.151 V (PCE of 18.84%) and the bottom sub-cell shows a V_{OC} of 0.685 V (PCE of 19.22%).

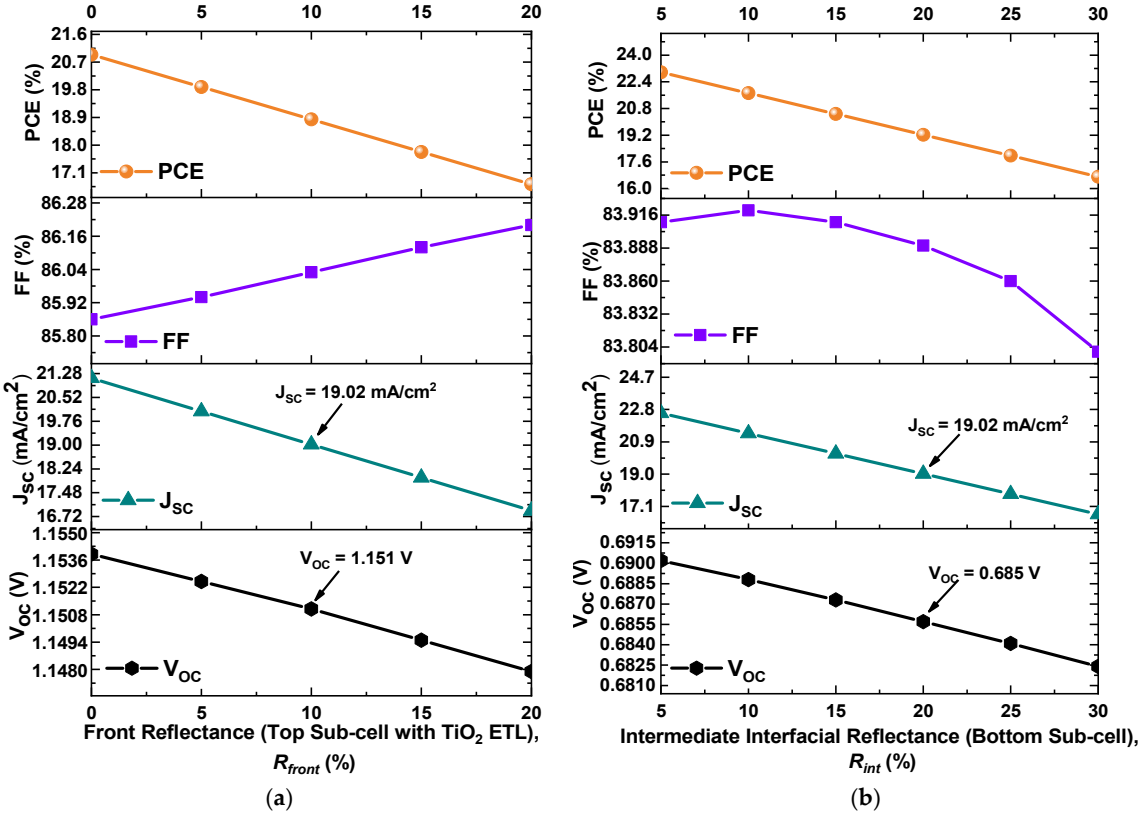

Figure 13. Effect of optical losses on the performance of tandem subcells: (**a**) Impact of R_{front} on the performance parameters of the top perovskite sub-cell (with a TiO_2 ETL and 200 nm of $CsSnBr_3$); (**b**) impact of R_{int} on the performance parameters of the bottom silicon sub-cell (278 µm). Arrows indicate the current matching point (19.02 mA/cm^2) at 10% R_{front} and 20% R_{int}.

A similar analysis was performed for the tandem configuration featuring an SnO_2 ETL, with the device optimized using a 200 nm $CsSnBr_3$ top sub-cell and a 265 µm silicon bottom sub-cell. Under the same conservative optical scenario (R_{front} = 10%, R_{int} = 20%), the J_{SC} of the top sub-cell decreased from 21.06 mA/cm^2 to 18.95 mA/cm^2, while the bottom sub-cell decreased from 22.51 mA/cm^2 to 18.95 mA/cm^2. As illustrated in Figure 14a,b, these conditions led to a precisely identified current matching point at 18.95 mA/cm^2. At this point, the SnO_2-based top sub-cell achieved a Voc of 1.151 V (PCE of 18.99%), while the bottom sub-cell reached a V_{OC} of 0.685 V and a PCE of 19.16%.

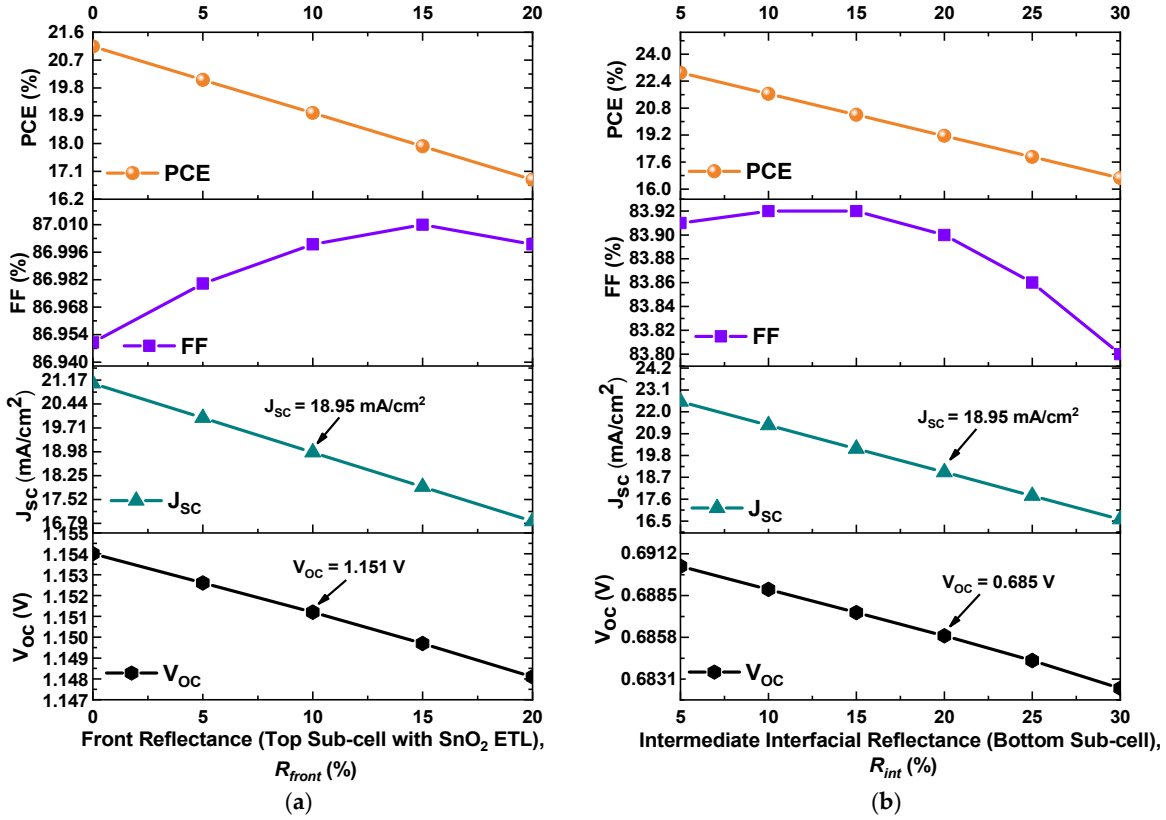

Figure 14. Effect of optical losses on the performance of tandem sub-cells. (**a**) Impact of R_{front} on the performance parameters of the top perovskite sub-cell (with a SnO_2 ETL and 200 nm of $CsSnBr_3$). (**b**) Impact of R_{int} on the performance parameters of the bottom silicon sub-cell (265 µm). Arrows indicate the current matching point (19.02 mA/cm^2) at 10% R_{front} and 20% R_{int}.

To validate this analysis under realistic conditions, a systematic stepwise optimization methodology was implemented. This approach rigorously accounts for optical reflectance losses in both the top sub-cell and the bottom silicon sub-cell. While the perovskite sub-cell was evaluated under the standard AM1.5G spectrum, the silicon sub-cell was simulated using the filtered transmitted spectrum. Current matching (J_{SC}) was achieved by varying the perovskite thickness from 100 to 700 nm while simultaneously optimizing the silicon thickness (200 to 300 µm) to synchronize both photovoltaic responses. As shown in Figure 15, the analysis identified an optimal configuration for both architectures. The TiO_2-based configuration (Figure 15a) achieved a J_{SC} matching of 19.02 mA/cm^2 using 200 nm of $CsSnBr_3$ and 278 µm of silicon. Similarly, the SnO_2-based configuration (Figure 15b) achieved a J_{SC} matching of 18.95 mA/cm^2 with a silicon thickness of 265 µm. These results demonstrate that robust performance and efficient charge synchronization are maintained even under interfacial optical limitations, regardless of the ETL material or slight variations in silicon thickness.

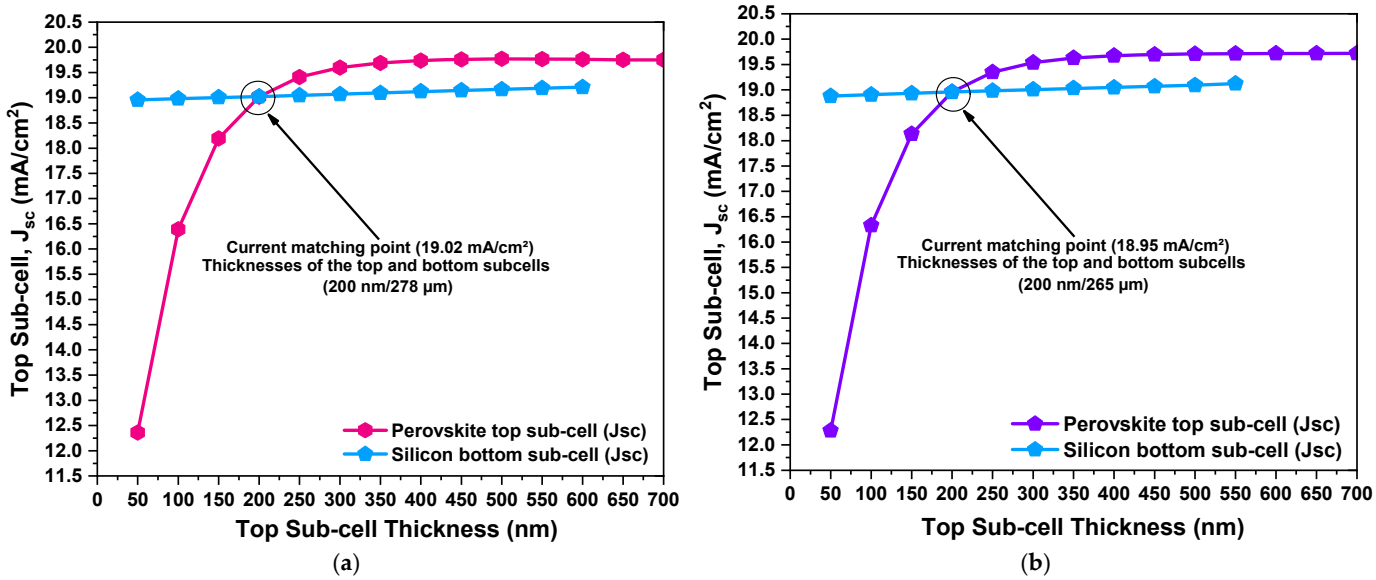

Figure 15. Current density-matching curves for the optimized tandem solar cell: (**a**) J_{SC} matching using TiO_2 ETL, identifying the optimal point at 19.02 mA/cm^2; (**b**) J_{SC} matching using a SnO_2 ETL, identifying the optimal point at 19.89 mA/cm^2.

3.7. Simulation of Lead-Free PVK-Si Tandem Solar Cells

The J-V characteristic curve of the lead-free PVK-Si tandem device was obtained through numerical interpolation of the individual sub cells' curves. The calculation was performed assuming a series-connection configuration, where the total device current is current-limited by the sub-cell with the lowest J_{SC} and the total voltage is the point-to-point summation of the individual voltages [5]. Table 2 summarizes the simulated performance parameters for the TiO_2-based perovskite top sub-cell and the bottom silicon sub-cell under various scenarios, including ideal conditions, thickness optimization, filtered spectrum, and optical reflectance losses. Finally, the overall efficiency of the tandem device, derived from these adjusted parameters, is presented.

Table 2. Simulated photovoltaic parameters of the TiO_2-based perovskite top sub-cell, silicon bottom sub-cell, and the resulting PVK-Si tandem device under different optimization and optical loss scenarios.

Scenario	Solar Cell Structure	V_{OC} (V)	J_{SC} (mA/cm^2)	FF (%)	PCE (%)
Ideal conditions	Perovskite top sub-cell	1.16	21.96	84.22	21.62
Ideal conditions	Silicon bottom sub-cell	0.70	39.40	84.32	23.48
R_{front} = 10%	Perovskite top sub-cell	1.16	19.77	84.32	19.46
R_{int} = 20%, Filtered spectrum	Silicon bottom sub-cell	0.68	18.56	83.92	18.78
R_{front} = 10%, 200 nm $CsSnBr_3$	Perovskite top sub-cell	1.15	19.02	86.03	18.84
R_{int} = 20%, 278 µm Silicon, Filtered spectrum	Silicon bottom sub-cell	0.68	19.02	83.89	19.22
Tandem Configuration	Lead free PVK-Si tandem solar cell	1.83	19.02	85.30	29.76

Similarly, Table 3 summarizes the simulated performance parameters for the SnO_2-based perovskite top sub-cell and the silicon bottom sub-cell under various scenarios. Finally, the overall efficiency of the tandem device, derived from these adjusted parameters, is presented.

Table 3. Simulated photovoltaic parameters of the SnO_2-based perovskite top sub-cell, silicon bottom sub-cell, and the resulting PVK-Si tandem device under different optimization and optical loss scenarios.

Scenario	Solar Cell Structure	V_{OC} (V)	J_{SC} (mA/cm^2)	FF (%)	PCE (%)
Ideal conditions	Perovskite top sub-cell	1.16	21.89	85.43	21.72
Ideal conditions	Silicon bottom sub-cell	0.70	39.40	84.32	23.48
R_{front} = 10%	Perovskite top sub-cell	1.15	19.70	85.47	19.50
R_{int} = 20%, Filtered spectrum	Silicon bottom sub-cell	0.68	18.48	83.92	18.71
R_{front} = 10%, 200 nm $CsSnBr_3$	Perovskite top sub-cell	1.15	18.95	87	18.99
R_{int} = 20%, 265 µm Silicon, Filtered spectrum	Silicon bottom sub-cell	0.68	18.95	83.90	19.16
Tandem Configuration	Lead free PVK-Si tandem solar cell	1.83	18.95	85.90	29.88

The final J-V characteristic curve of the lead-free TiO_2-based PVK-Si tandem device is shown in Figure 16a, which achieved a J_{SC} of 19.02 mA/cm^2, a V_{OC} of 1.83 V, an FF of 85.30%, and a global PCE of 29.76%. Similarly, the final J-V characteristic curve for the lead-free SnO_2-based PVK-Si tandem device is shown in Figure 16b, which achieved a J_{SC} of 18.95 mA/cm^2, a V_{OC} of 1.83 V, an FF of 85.90%, and a global PCE of 29.88%. These results demonstrate that both tandem configurations remain highly efficient even after accounting for cumulative optical losses.

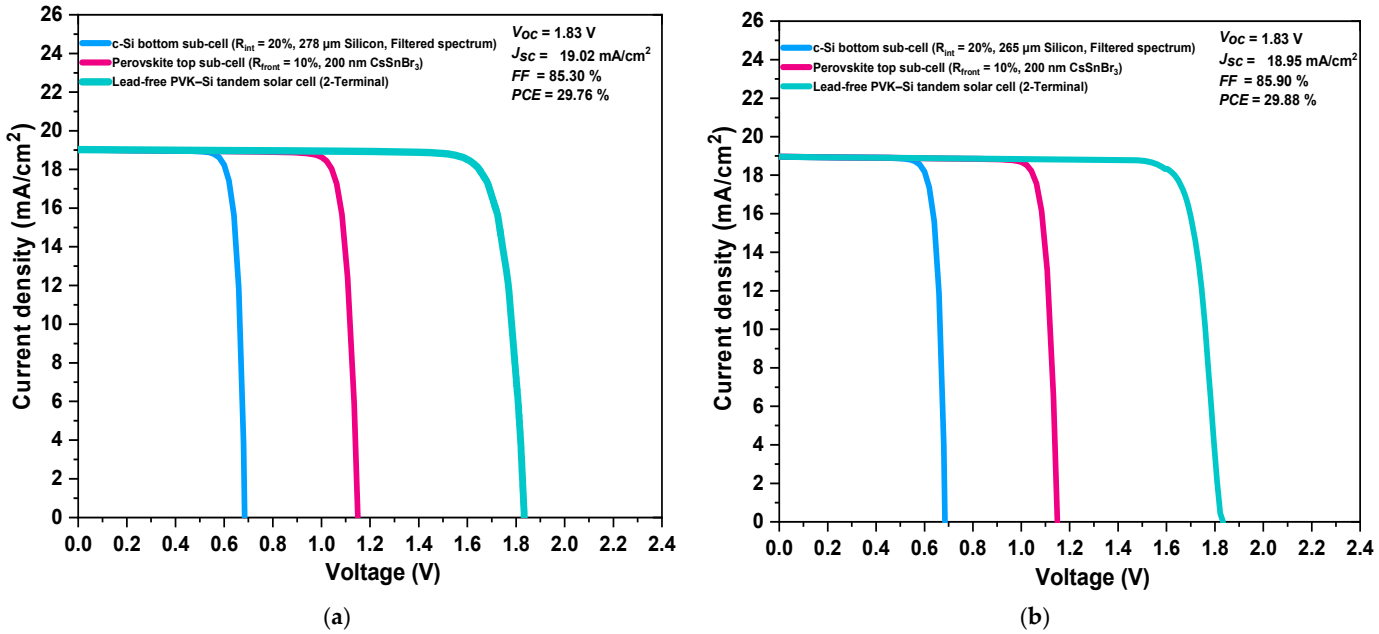

Figure 16. Current density (J-V) characteristics of the monolithic lead-free PVK-Si tandem solar cells featuring (**a**) a TiO_2-based and (**b**) a SnO_2-based electron transport layer.

Figure 17 shows the External Quantum Efficiency (EQE) of the lead-free TiO_2-based PVK-Si tandem device. A complementary spectral response is observed, where the top perovskite sub-cell absorbs in the 300–700 nm range, while the bottom silicon sub-cell harnesses low-energy photons up to 1200 nm. The EQE peak of 93.10% in the near-infrared region confirms the high transparency of the FTO/TiO_2/$CsSnBr_3$/rGO stack, enabling optimal light transmission and a matched current density of 19.02 mA/cm^2.

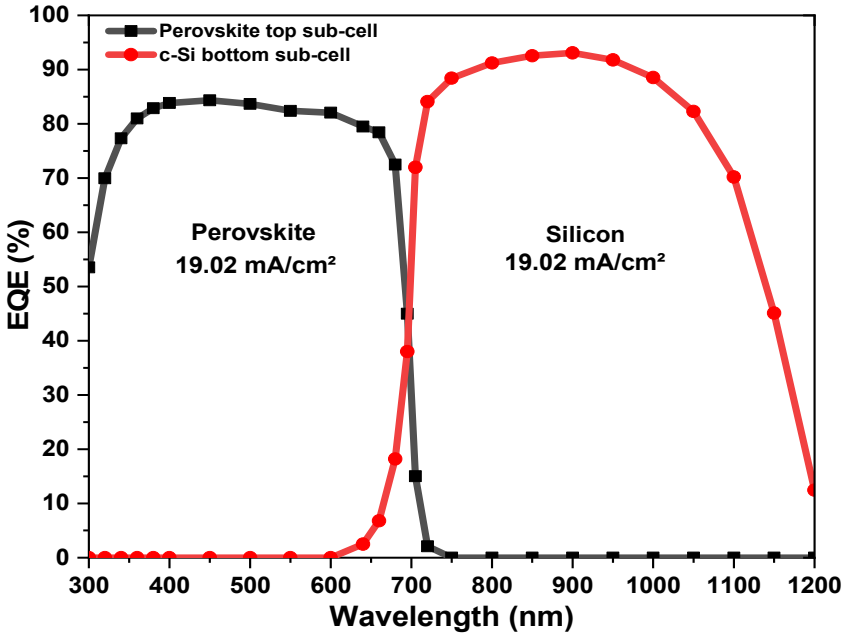

Figure 17. EQE of the monolithic lead-free PVK-Si tandem solar cells with a TiO_2-based electron transport layer.

3.8. Comparison Between Experiment and Simulation

Table 4 presents a comparison of the photovoltaic performance of our proposed lead-free PVK-Si tandem device against two benchmarks: (1) simulation reports of lead-free PVK-Si tandem cells with similar structures, and (2) experimental reports of PVK-Si tandem cells with lead.

Table 4. Comparison of the photovoltaic performance of the proposed lead-free PVK-Si tandem solar cell with reports from the literature.

Solar Cell Structure	V_{OC} (V)	J_{SC} (mA/cm^2)	FF (%)	PCE (%)	Ref.
$Cs_{0.22}FA_{0.78}Pb(Br_{0.15}I_{0.85})_3$/Silicon Tandem Solar Cell (Experimental)	1.794	19.68	78.27	27.60	[59]
$Cs_{0.05}(FA_{0.83}MA_{0.17})_{0.95}Pb(Br_{0.17}I_{0.83})_3$/Silicon Tandem Solar Cell (Experimental)	1.80	19.3	81.9	28.50	[60]
$FA_{0.78}Cs_{0.22}Pb(I_{0.85}Br_{0.15})_3$/Silicon Tandem Solar Cell (Experimental)	1.91	19.29	82.5	28.7	[61]
$Cs_{0.22}FA_{0.78}Pb(I_{0.85}Br_{0.15})_3$ +5% $MAPbCl_3$/Silicon Tandem Solar Cell (Experimental)	2.0	20.24	81.18	32.5	[62]
$Cs_{0.05}FA_{0.8}MA_{0.15}PbI_{2.27}Br_{0.73}$/Silicon Tandem Solar Cell (Experimental)	1.95	20.94	80.78	33.03	[58]
$MAPbI_3$/Silicon Tandem Solar Cell (Simulation)	1.88	19.96	85.99	32.29	[18]
Lead- Free $CsSn_{0.5}Ge_{0.5}I_3$/Silicon Tandem Solar Cell (Simulation)	1.72	20.02	83.74	28.53	[18]
Lead- Free $MAGeI_3$/silicon Tandem Solar Cell (Simulation)	2.06	16.2	85.9	28.71	[17]
Lead-Free $CsSnBr_3$/Silicon Tandem Solar Cell (TiO_2 ETL) (Simulation)	1.83	19.02	85.30	29.76	This work
Lead-Free $CsSnBr_3$/Silicon Tandem Solar Cell (SnO_2 ETL) (Simulation)	1.83	18.95	85.90	29.88	This work

Notably, the performance of the proposed architecture was further evaluated by comparing two different ETLs. While the TiO_2-based tandem device achieved a PCE of

29.76%, the implementation of a SnO_2 layer enhanced the FF to 85.90%, resulting in a maximum efficiency of 29.88%. This slight advantage of the SnO_2 configuration suggests a more efficient charge extraction at the perovskite/ETL interface, reinforcing the potential of this lead-free design to rival existing benchmarks in the literature.

4. Conclusions

This study modelled a two-terminal, lead-free PVK-Si tandem solar cell that achieved an efficiency exceeding 30%. The device structure consisted of a top sub-cell that utilized $CsSnBr_3$ as the absorbing material with an optimized bandgap of 1.78 eV, and a bottom sub-cell that utilized silicon as the absorbing material with a bandgap of 1.12 eV. Prior to the tandem device simulation, both sub-cells were numerically optimized under standard AM1.5G 1-sun illumination, achieving efficiencies of 21.62% and 23.48%, respectively. The optimized top sub-cell (FTO/TiO_2/$CsSnBr_3$/rGO/Au) had a $CsSnBr_3$ thickness of 500 nm, a TiO_2 thickness of 40 nm, an rGO thickness of 50 nm, an N_t for $CsSnBr_3$ of 10^{14} cm^{-3}, an N_t for both interfaces of 10^{13} cm^{-2}, and a bandgap for $CsSnBr_3$ of 1.78 eV. The tandem device simulation employed realistic operating conditions, with the top sub-cell being illuminated by the standard AM1.5G 1-sun spectrum, and the bottom sub-cell received the solar spectrum filtered through the top perovskite sub-cell. To ensure a realistic simulation, cumulative optical losses were incorporated by assuming a front reflectance and an intermediate interfacial reflectance. Subsequently, the series connection of the sub-cells was obtained by matching the current densities and adding voltages. This was achieved with a thickness of 200 nm for $CsSnBr_3$ and a thickness of 278 μm for silicon. Consequently, the resulting matched J_{SC} value was 19.02 mA/cm^2. The complete FTO/TiO_2/$CsSnBr_3$/rGO/TCO(ITO)/c-Si(n)/c-Si(p)/c-Si(p+)/Al configuration exhibited excellent performance metrics. Specifically, the device utilizing a TiO_2 ETL achieved a PCE of 29.76% (FF of 85.30%), while the SnO_2-based configuration further optimized the performance, reaching a PCE of 29.88% due to an enhanced FF of 85.90%. The EQE response demonstrates efficient photon management through complementary absorption by the sub-cells, resulting in optimized carrier collection across the entire solar spectrum. The performance achieved by our proposed device is competitive with conventionally manufactured and simulated PVK-Si 2T tandem devices. In the absence of existing lead-free experimental devices, the present study proposes a feasible approach for the development of non-toxic, cost-effective tandem solar systems suitable for large-scale manufacturing.

Author Contributions: Conceptualization, J.A.L.L. and M.M.M.; methodology, E.P.T. and M.M.M.; software, E.P.T. and A.C.P.R.; validation, A.M.S., J.C.L. and Z.J.H.S.; formal analysis, E.P.T. and J.A.L.L.; investigation, G.O.M.C., J.F.M. and L.H.M.; resources, J.F.M. and A.C.P.R.; data curation, E.P.T., Z.J.H.S. and M.M.M.; writing—original draft preparation, E.P.T.; writing—review and editing, E.P.T. and M.M.M.; visualization, J.C.L. and G.O.M.C.; supervision, A.M.S. and L.H.M.; project administration, J.F.M. and A.C.P.R.; funding acquisition, J.A.L.L. and J.F.M. All authors have read and agreed to the published version of the manuscript.

Funding: This research received no external funding.

Data Availability Statement: The original contributions presented in this study are included in the article. Further inquiries can be directed to the corresponding author.

Acknowledgments: The authors express their gratitude to SECIHTI, INAOE, and CIDS-BUAP for the institutional and technical support provided during the development of this work.

Conflicts of Interest: The authors declare no conflicts of interest.

References

1. Earis, P.; Nugent, N.; Martinez-fresno, M.; Wilkes, S.; Spring, S.; Dean, J.; Lewis, N.; Berkeley, U.C.; Bolt, H. Exceeding the Shockley–Queisser Limit in Solar Energy Conversion. *Energy Environ. Sci.* **2013**, *6*, 3508–3519. [CrossRef]
2. Green, M.A.; Dunlop, E.D.; Siefer, G.; Yoshita, M.; Kopidakis, N.; Bothe, K.; Hao, X. Solar Cell Efficiency Tables (Version 61). *Prog. Photovolt. Res. Appl.* **2023**, *31*, 3–16. [CrossRef]
3. Bati, A.S.R.; Zhong, Y.L.; Burn, P.L.; Nazeeruddin, M.K.; Shaw, P.E.; Batmunkh, M. Next-Generation Applications for Integrated Perovskite Solar Cells. *Commun. Mater.* **2023**, *4*, 2. [CrossRef]
4. Wang, P.; Li, W.; Sandberg, O.J.; Guo, C.; Sun, R.; Wang, H.; Li, D.; Zhang, H.; Cheng, S.; Liu, D.; et al. Tuning of the Interconnecting Layer for Monolithic Perovskite/Organic Tandem Solar Cells with Record Efficiency Exceeding 21%. *Nano Lett.* **2021**, *21*, 7845–7854. [CrossRef] [PubMed]
5. Ying, Z.; Yang, X.; Wang, X.; Ye, J. Towards the 10-Year Milestone of Monolithic Perovskite/Silicon Tandem Solar Cells. *Adv. Mater.* **2024**, *36*, 2311501. [CrossRef]
6. Schileo, G.; Grancini, G. Lead or No Lead? Availability, Toxicity, Sustainability and Environmental Impact of Lead-Free Perovskite Solar Cells. *J. Mater. Chem. C* **2021**, *9*, 67–76. [CrossRef]
7. Khodair, D.; Saeed, A.; Shaker, A.; Abouelatta, M.; Abdelraouf, O.A.M.; EL-Rabaie, S. A Review on Tandem Solar Cells Based on Perovskite/Si: 2-T versus 4-T Configurations. *Sol. Energy* **2025**, *300*, 113815. [CrossRef]
8. Liang, Y.; Cui, X.; Li, F.; Stampfl, C.; Ringer, S.P.; Zheng, R. Electrode-Induced Impurities in Tin Halide Perovskite Solar Cell Material $CsSnBr_3$ from First Principles. *npj Comput. Mater.* **2021**, *7*, 63. [CrossRef]
9. Karmakar, A.; Bhattacharya, A.; Sarkar, D.; Bernard, G.M.; Mar, A.; Michaelis, V.K. Influence of Hidden Halogen Mobility on Local Structure of $CsSn(Cl_{1-x}Br_x)_3$ mixed-Halide Perovskites by Solid-State NMR. *Chem. Sci.* **2021**, *12*, 3253–3263. [CrossRef]
10. Gupta, S.; Bendikov, T.; Hodes, G.; Cahen, D. $CsSnBr_3$, A Lead-Free Halide Perovskite for Long-Term Solar Cell Application: Insights on SnF_2 Addition. *ACS Energy Lett.* **2016**, *1*, 1028–1033. [CrossRef]
11. Jacob Olasoji, A.; Hyuk Im, S. Perspective Chapter: TiO_2 Electron Transporting Layers for Perovskite Solar Cells. In *Titanium Dioxide—Uses, Applications, and Advances*; IntechOpen: London, UK, 2024; Volume 3. [CrossRef]
12. Suragtkhuu, S.; Tserendavag, O.; Vandandoo, U.; Bati, A.S.R.; Bat-Erdene, M.; Shapter, J.G.; Batmunkh, M.; Davaasambuu, S. Efficiency and Stability Enhancement of Perovskite Solar Cells Using Reduced Graphene Oxide Derived from Earth-Abundant Natural Graphite. *RSC Adv.* **2020**, *10*, 9133–9139. [CrossRef] [PubMed]
13. Yang, Q.D.; Li, J.; Cheng, Y.; Li, H.W.; Guan, Z.; Yu, B.; Tsang, S.W. Graphene Oxide as an Efficient Hole-Transporting Material for High-Performance Perovskite Solar Cells with Enhanced Stability. *J. Mater. Chem. A* **2017**, *5*, 9852–9858. [CrossRef]
14. Mondol, N.; Islam, K.S.; Islam, M.R.; Das, S.K. Enhancing Solar Cell Efficiency: Investigation of High-Performance Lead-Based Perovskite-on-Silicon (PVK-Si) Tandem Solar Cells through Design and Numerical Analysis. *AIP Adv.* **2024**, *14*, 015110. [CrossRef]
15. Ahmed, M.S.; Ahmad, S.M.; Subhyaljader, M. Study the Role of Effective Parameters in Enhancement of the Silicon Solar Cell Performance Using PC1D Simulation. *J. Ovonic Res.* **2020**, *16*, 97–106. [CrossRef]
16. Thirunavukkarasu, G.S.; Seyedmahmoudian, M.; Chandran, J.; Stojcevski, A.; Subramanian, M.; Marnadu, R.; Alfaify, S.; Shkir, M. Optimization of Mono-Crystalline Silicon Solar Cell Devices Using PC1D Simulation. *Energies* **2021**, *14*, 4986. [CrossRef]
17. Sarker, S.; Islam, M.T.; Rauf, A.; Al Jame, H.; Jani, M.R.; Ahsan, S.; Islam, M.S.; Nishat, S.S.; Shorowordi, K.M.; Ahmed, S. A SCAPS Simulation Investigation of Non-Toxic $MAGeI_3$-on-Si Tandem Solar Device Utilizing Monolithically Integrated (2-T) and Mechanically Stacked (4-T) Configurations. *Sol. Energy* **2021**, *225*, 471–485. [CrossRef]
18. Islam, M.T.; Jani, M.R.; Islam, A.F.; Shorowordi, K.M.; Chowdhury, S.; Nishat, S.S.; Ahmed, S. Investigation of $CsSn_{0.5}Ge_{0.5}I_3$-on-Si Tandem Solar Device Utilizing SCAPS Simulation. *IEEE Trans. Electron Devices* **2021**, *68*, 618–625. [CrossRef]
19. Huang, J.; Mao, L. A Review on Perovskite/Silicon Tandem Solar Cells: Current Status and Future Challenges. *Energies* **2025**, *18*, 4327. [CrossRef]
20. Moinuddin, R.M.; Hasan, M.; Rahaman, M.; Islam, K.S. Numerical Optimization and Efficiency Analysis of Sn-Based Perovskite-on-Silicon Tandem Solar Cells with Various TCO Materials Using SCAPS-1D Simulation. *AIP Adv.* **2024**, *14*, 085126. [CrossRef]
21. Burgelman, M.; Decock, K.; Niemegeers, A.; Verschraegen, J.; Degrave, S. SCAPS-1D Manual. 2025. Available online: https://scaps.elis.ugent.be/SCAPS%20manual%20most%20recent.pdf (accessed on 20 April 2026).
22. Burgelman, M.; Nollet, P.; Degrave, S. Modelling Polycrystalline Semiconductor Solar Cells. *Thin Solid Films* **2000**, *361*, 527–532. [CrossRef]
23. Hulstrom, R.; Bird, R.; Riordan, C. Spectral Solar Irradiance Data Sets for Selected Terrestrial Conditions. *Sol. Cells* **1985**, *15*, 365–391. [CrossRef]
24. Sarker, S.; Islam, M.T.; Rauf, A.; Al Jame, H.; Ahsan, S.; Islam, M.S.; Jani, M.R.; Nishat, S.S.; Shorowordi, K.M.; Ahmed, S. A Simulation Based Incremental Study of Stable Perovskite-on-Perovskite Tandem Solar Device Utilizing Non-Toxic Tin and Germanium Perovskite. *Mater. Today Commun.* **2022**, *32*, 103881. [CrossRef]
25. Shrivastav, N.; Madan, J.; Pandey, R.; Shalan, A.E. Investigations Aimed at Producing 33% Efficient Perovskite-Silicon Tandem Solar Cells through Device Simulations. *RSC Adv.* **2021**, *11*, 37366–37374. [CrossRef]

26. Karthick, S.; Velumani, S.; Bouclé, J. Experimental and SCAPS Simulated Formamidinium Perovskite Solar Cells: A Comparison of Device Performance. *Sol. Energy* **2020**, *205*, 349–357. [CrossRef]
27. Rai, S.; Pandey, B.K.; Dwivedi, D.K. Device Simulation of Low Cost HTM Free Perovskite Solar Cell Based on TiO_2 electron Transport Layer. *AIP Conf. Proc.* **2020**, *2220*, 140022. [CrossRef]
28. Dar, S.A.; Sengar, B.S. Optimization and Performance Analysis of Inorganic Lead-Free $CsSnBr_3$ Perovskite Solar Cells Using Diverse Electron Transport Materials. *Energy Fuels* **2024**, *38*, 8229–8248. [CrossRef]
29. Karna, L.R.; Upadhyay, R.; Ghosh, A. All-Inorganic Perovskite Photovoltaics for Power Conversion Efficiency of 31%. *Sci. Rep.* **2023**, *13*, 15212. [CrossRef]
30. Kheswa, B.V. Numerical Optimization of All-Inorganic $CsSnBr_3$ Perovskite Solar Cells: The Observation of 27% Power Conversion Efficiency. *Phys. Scr.* **2025**, *100*, 015933. [CrossRef]
31. Afrasiab; Khan, A.D.; Subhan, F.E.; Khan, A.D.; Khan, S.D.; Ahmad, M.S.; Rehan, M.S.; Noman, M. Optimization of Efficient Monolithic Perovskite/Silicon Tandem Solar Cell. *Optik* **2020**, *208*, 164573. [CrossRef]
32. Shawky, T.; Aly, M.H.; Fedawy, M. Performance Analysis and Simulation of C-Si/SiGe Based Solar Cell. *IEEE Access* **2021**, *9*, 75283–75292. [CrossRef]
33. Sehili, A.; Nora, O. Numerical Modeling and Performance Optimization of an $FTO/SnO_2/Cs_2AgBiBr_6/NiO/Pt$ Double Perovskite Solar Cell Using SCAPS-1D. *ChemistrySelect* **2026**, *11*, e06430. [CrossRef]
34. Das, B.; Liu, Z.; Aguilera, I.; Rau, U.; Kirchartz, T. Defect Tolerant Device Geometries for Lead-Halide Perovskites. *Mater. Adv.* **2021**, *2*, 3655–3670. [CrossRef]
35. Buratti, Y.; Le Gia, Q.T.; Dick, J.; Zhu, Y.; Hameiri, Z. Extracting Bulk Defect Parameters in Silicon Wafers Using Machine Learning Models. *npj Comput. Mater.* **2020**, *6*, 142. [CrossRef]
36. Fujiwara, H.; Collins, R.W. *Spectroscopic Ellipsometry for Photovoltaics Volume 1: Fundamental Principles and Solar Cell Characterization*; Springer: Cham, Swizterland, 2018; Volume 2.
37. Fujiwara, H.; Collins, R.W. *Spectroscopic Ellipsometry for Photovoltaics Volume 2: Applications and Optical Data of Solar Cell Materials*; Springer: Cham, Swizterland, 2018; Volume 58.
38. Pandey, M.; Hamal, D.; Subedi, D.; Basnet, B.; Sah, R.; Tiwari, S.K.; Kafle, B. Deposition of Reduced Graphene Oxide Thin Film by Spray Pyrolysis Method for Perovskite Solar Cell. *J. Nepal Phys. Soc.* **2021**, *7*, 53–58. [CrossRef]
39. Khatoon, S.; Kumar Yadav, S.; Chakraborty, V.; Singh, J.; Bahadur Singh, R. A Simulation Study of All Inorganic Lead-Free $CsSnBr_3$ Tin Halide Perovskite Solar Cell. *Mater. Today Proc.* 2023; *in press*. [CrossRef]
40. Kheswa, B.V.; Majola, S.N.T. Simulation of Novel $CsSnBr_3$ Perovskite Solar Cells Achieving Efficiency of 31.62%. *Phys. Scr.* **2025**, *100*, 015017. [CrossRef]
41. Rai, S.; Pandey, B.K.; Dwivedi, D.K. Modeling of Highly Efficient and Low Cost $CH_3NH_3Pb(I_{1-X}Cl_x)_3$ Based Perovskite Solar Cell by Numerical Simulation. *Opt. Mater.* **2020**, *100*, 109631. [CrossRef]
42. Ali, A.; Zulfiqar, M.; Bano, N.; Hussain, I.; Asif, S.U. Examining Compatible Electron Transport Layers for $CsSnBr_3$-Based Solar Cell to Boost Photovoltaic Stability and Efficiency. *Energy Technol.* **2024**, *12*, 2400632. [CrossRef]
43. Jamal, M.S.; Shahahmadi, S.A.; Chelvanathan, P.; Asim, N.; Misran, H.; Hossain, M.I.; Amin, N.; Sopian, K.; Akhtaruzzaman, M. Effect of Defect Density and Energy Level Mismatch on the Performance of Perovskite Solar Cells by Numerical Simulation. *Optik* **2019**, *182*, 1204–1210. [CrossRef]
44. Sławek, A.; Starowicz, Z.; Lipinski, M. The Influence of the Thickness of Compact TiO_2 Electron Transport Layer on the Performance of Planar $CH_3NH_3PbI_3$ Perovskite Solar Cells. *Materials* **2021**, *14*, 3295. [CrossRef]
45. Masood, M.T.; Weinberger, C.; Sarfraz, J.; Rosqvist, E.; Sandén, S.; Sandberg, O.J.; Vivo, P.; Hashmi, G.; Lund, P.D.; Österbacka, R.; et al. Impact of Film Thickness of Ultrathin Dip-Coated Compact TiO_2 Layers on the Performance of Mesoscopic Perovskite Solar Cells. *ACS Appl. Mater. Interfaces* **2017**, *9*, 17906–17913. [CrossRef] [PubMed]
46. Sosa-Acosta, J.R.; Villarroel, R.; Cerda, D.; Ruiz, C.; Fernández-Izquierdo, L.; Peón-Díaz, F.J.; Navarrete-Astorga, E.; Leinen, D.; del Río, R.; Hevia, S.A. Compact TiO_2 film Thickness Optimization and Its Effect on $CsPbBr_3$-Based Photoanode Performance for Oxygen Evolution Reaction. *J. Power Sources* **2026**, *662*, 238805. [CrossRef]
47. Yadav, S.; Gupta, S.K.; Negi, C.M.S. Graphene Derivatives as Efficient Hole Transport Materials for Lead-Free Double Perovskite (Cs_2SnI_6) Solar Cells: A Numerical Study. *Optoelectron. Lett.* **2025**, *21*, 155–159. [CrossRef]
48. Hasan, M.A. Highly Stable Perovskite Solar Cells Using Graphene and Its Derivatives: A Review. *Adv. Mater. Interfaces* **2026**, *13*, e00855. [CrossRef]
49. Lee, H.; Li, D. Surface Passivation to Improve the Performance of Perovskite Solar Cells. *Energies* **2024**, *17*, 5282. [CrossRef]
50. Basyoni, M.S.S.; Salah, M.M.; Mousa, M.; Shaker, A.; Zekry, A.; Abouelatta, M.; Alshammari, M.T.; Al-Dhlan, K.A.; Gontrand, C. On the Investigation of Interface Defects of Solar Cells: Lead-Based vs Lead-Free Perovskite. *IEEE Access* **2021**, *9*, 130221–130232. [CrossRef]
51. Shockley, W.; Read, W.T. Statistics of the Recombinations of Holes and Electrons. *Phys. Rev.* **1952**, *87*, 835–842. [CrossRef]

52. Miah, M.H.; Khandaker, M.U.; Rahman, M.B.; Nur-E-Alam, M.; Islam, M.A. Band Gap Tuning of Perovskite Solar Cells for Enhancing the Efficiency and Stability: Issues and Prospects. *RSC Adv.* **2024**, *14*, 15876–15906. [CrossRef] [PubMed]
53. Yu, M.L.; Los, A.; Xiong, G. Thin Film Absorbers for Tandem Solar Cells: An Industrial Perspective. *J. Phys. Energy* **2023**, *5*, 042002. [CrossRef]
54. Sabba, D.; Mulmudi, H.K.; Prabhakar, R.R.; Krishnamoorthy, T.; Baikie, T.; Boix, P.P.; Mhaisalkar, S.; Mathews, N. Impact of Anionic Br- Substitution on Open Circuit Voltage in Lead Free Perovskite ($CsSnI_{3-X}Br_X$) Solar Cells. *J. Phys. Chem. C* **2015**, *119*, 1763–1767. [CrossRef]
55. Ullah, S.; Rasheed J., F.; Khan, F.; Ali, A. Performance Analysis of Nontoxic $CsSnI_2Br$-Based Perovskite Solar Cells: Insights from SCAPS-1D Simulations. *ACS Appl. Eng. Mater.* **2025**, *3*, 4641–4655. [CrossRef]
56. Fang, D.; Tong, Y.; Xu, F.; Mi, B.; Cao, D.; Gao, Z. Preparation of $CsSnBr_3$ Perovskite Film and Its All-Inorganic Solar Cells with Planar Heterojunction. *J. Solid State Chem.* **2021**, *294*, 6–11. [CrossRef]
57. Wang, X.; Wang, W.; Liu, J.; Qi, J.; He, Y.; Wang, Y.; Hu, W.; Cheng, Y.; Chen, K.; Hu, Y.; et al. Reducing Optical Reflection Loss for Perovskite Solar Cells Via Printable Mesoporous SiO_2 Antireflection Coatings. *Adv. Funct. Mater.* **2022**, *32*, 2203872. [CrossRef]
58. Zhang, D.; Wu, T.; Li, B.; Ding, D.; Li, R.; Wei, J.; Zhang, H.; Kan, C.; Yao, Y.; Hang, P.; et al. Iceberg-like Pyramids in Industrially Textured Silicon Enabled 33% Efficient Perovskite-Silicon Tandem Solar Cells. *Nat. Commun.* **2025**, *16*, 7331. [CrossRef]
59. Wu, Y.; Zheng, P.; Peng, J.; Xu, M.; Chen, Y.; Surve, S.; Lu, T.; Bui, A.D.; Li, N.; Liang, W.; et al. 27.6% Perovskite/c-Si Tandem Solar Cells Using Industrial Fabricated TOPCon Device. *Adv. Energy Mater.* **2022**, *12*, 2200821. [CrossRef]
60. Ying, Z.; Yang, Z.; Zheng, J.; Wei, H.; Chen, L.; Xiao, C.; Sun, J.; Shou, C.; Qin, G.; Sheng, J.; et al. Monolithic Perovskite/Black-Silicon Tandems Based on Tunnel Oxide Passivated Contacts. *Joule* **2022**, *6*, 2644–2661. [CrossRef]
61. Sveinbjörnsson, K.; Li, B.; Mariotti, S.; Jarzembowski, E.; Kegelmann, L.; Wirtz, A.; Frühauf, F.; Weihrauch, A.; Niemann, R.; Korte, L.; et al. Monolithic Perovskite/Silicon Tandem Solar Cell with 28.7% Efficiency Using Industrial Silicon Bottom Cells. *ACS Energy Lett.* **2022**, *7*, 2654–2656. [CrossRef]
62. Mariotti, S.; Köhnen, E.; Scheler, F.; Sveinbjörnsson, K.; Zimmermann, L.; Piot, M.; Yang, F.; Li, B.; Warby, J.; Musiienko, A.; et al. Interface Engineering for High-Performance, Triple-Halide Perovskite–Silicon Tandem Solar Cells. *Science* **2023**, *381*, 63–69. [CrossRef] [PubMed]